



Selective autophagy of RIPosomes maintains innate immune homeostasis during bacterial infection

Subhash Mehto^{1,*†} , Kautilya Kumar Jena^{1,†,‡} , Rina Yadav^{1,2}, Swatishmita Priyadarsini³, Pallavi Samal¹, Sivaram Krishna^{1,2} , Kollori Dhar^{1,2}, Ashish Jain^{4,5} , Nishant Ranjan Chauhan¹ , Krushna C Murmu⁶ , Ramyasingh Bal^{1,7}, Rinku Sahu^{1,2} , Pundrik Jaiswal¹, Bhabani Sankar Sahoo³, Srinivas Patnaik⁷, Thomas A Kufer⁸ , Tor Erik Rusten^{4,5} , Swati Chauhan⁶, Punit Prasad⁶ & Santosh Chauhan^{1,9,**}

Abstract

The NOD1/2-RIPK2 is a key cytosolic signaling complex that activates NF- κ B pro-inflammatory response against invading pathogens. However, uncontrolled NF- κ B signaling can cause tissue damage leading to chronic diseases. The mechanisms by which the NODs-RIPK2-NF- κ B innate immune axis is activated and resolved remain poorly understood. Here, we demonstrate that bacterial infection induces the formation of endogenous RIPK2 oligomers (RIPosomes) that are self-assembling entities that coat the bacteria to induce NF- κ B response. Next, we show that autophagy proteins IRGM and p62/SQSTM1 physically interact with NOD1/2, RIPK2 and RIPosomes to promote their selective autophagy and limit NF- κ B activation. IRGM suppresses RIPK2-dependent pro-inflammatory programs induced by *Shigella* and *Salmonella*. Consistently, the therapeutic inhibition of RIPK2 ameliorates *Shigella* infection- and DSS-induced gut inflammation in Irgm1 KO mice. This study identifies a unique mechanism where the innate immune proteins and autophagy machinery are recruited together to the bacteria for defense as well as for maintaining immune homeostasis.

Keywords autophagy; inflammation; Irgm1; NOD1/2-RIPK2-NF- κ B; RIPosomes

Subject Categories Autophagy & Cell Death; Microbiology, Virology & Host Pathogen Interaction

DOI 10.15252/emboj.2022111289 | Received 28 March 2022 | Revised 12 September 2022 | Accepted 15 September 2022 | Published online 11 October 2022

The EMBO Journal (2022) 41: e111289

Introduction

NOD1 and NOD2 (NODs) are cytosolic pattern recognition receptors (PRRs) that detect pathogen-associated molecular patterns (PAMPs), iE-DAP (D-glutamyl-meso-diaminopimelic acid), and MDP (muramyl dipeptide; Tanabe *et al*, 2004; Laroui *et al*, 2011; Caruso *et al*, 2014). Stimulated NODs interact and activate adaptor protein RIPK2 (RICK, RIP2) for a cascade of events resulting in NF- κ B activation and pro-inflammatory cytokine release (Girardin *et al*, 2001; Caruso *et al*, 2014). NODs-RIPK2 is one of the major innate immune axis that senses intracellular bacterial pathogens and mounts a powerful NF- κ B-dependent pro-inflammatory cytokine response to eliminate bacteria.

An important step for triggering pro-inflammatory innate immune pathways is the oligomerization of PRRs and/or adaptor proteins (Hou *et al*, 2011; Xie *et al*, 2013; Xu *et al*, 2014; Wu & Fuxreiter, 2016). For example, activation of RIG-I signaling induces polymerization of MAVS to form detergent-resistant, protease-resistant, and self-perpetuating prion-like aggregates (filamentous structure) to activate and transmit antiviral signaling (Hou *et al*, 2011; Cai *et al*, 2014; Wu *et al*, 2014; Xu *et al*, 2014). The inflammasome is another classical example, where several self-polymerized inflammatory proteins interact with each other to form multiprotein signalosomes that execute pro-inflammatory responses (Cai *et al*, 2014; Lu *et al*, 2014, 2016). Recently, structural studies demonstrated that purified RIPK2 polymerizes to form filamentous structures that are important for NODs-dependent NF- κ B signaling (Gong *et al*, 2018; Pellegrini *et al*, 2018). Also, ectopically

1 Cell Biology and Infectious Diseases Unit, Department of Infectious Disease Biology, Institute of Life Sciences, Bhubaneswar, India

2 Regional Centre for Biotechnology, NCR Biotech Science Cluster, Faridabad, India

3 Institute of Life Sciences, Bhubaneswar, India

4 Centre for Cancer Cell Reprogramming, Institute of Clinical Medicine, Faculty of Medicine, University of Oslo, Oslo, Norway

5 Department of Molecular Cell Biology, Institute for Cancer Research, Oslo University Hospital, Oslo, Norway

6 Epigenetic and Chromatin Biology Unit, Institute of Life Sciences, Bhubaneswar, India

7 School of Biotechnology, KIIT University, Bhubaneswar, India

8 Department of Immunology, Institute of Nutritional Medicine, University of Hohenheim, Stuttgart, Germany

9 CSIR-Centre For Cellular And Molecular Biology (CCMB), Hyderabad, India

*Corresponding author. Tel: +91 7503157368; E-mail: subhash@ils.res.in

**Corresponding author. Tel: +91 7077702598; E-mail: schauhan@ils.res.in; schauhan@ccmb.res.in

†These authors contributed equally to this work

‡Present address: Division of Immunology, Boston Children's Hospital, Harvard Medical School, Boston, MA, USA

expressed RIPK2 was shown to form detergent-insoluble higher-order oligomeric structures upon *Shigella* infection (Ellwanger et al, 2019). These structures were termed “RIPosomes.” To date, it is not clear whether endogenous RIPK2 forms RIPosomes and if yes, how they regulate NF- κ B signaling upon bacterial infection.

The NODs-RIPK2-NF- κ B pro-inflammatory axis is critical for clearing pathogens; however, its aberrant activation can cause chronic inflammation, oncogenesis, and autoimmune disease (Miceli-Richard et al, 2001; Kanazawa et al, 2005; Henckaerts & Vermeire, 2007; Caso et al, 2015; Taniguchi & Karin, 2018). To avoid these conditions, a balanced immune state needs to be maintained by negative feedback mechanisms. Inflammophagy, the autophagic degradation of inflammatory aggregates and proteins, is an emerging mechanism to limit inflammation to maintain innate immune homeostasis (Chauhan et al, 2021; Deretic, 2021). Several of the cytosolic PRRs and adaptor proteins including RIG-I, NLRP3, AIM2, cGAS, MAVS, and STING are targeted by p62- or NDP52-dependent selective autophagy to dampen the excess inflammation (Shi et al, 2012; Liu et al, 2016; Du et al, 2018; Prabakaran et al, 2018; He et al, 2019; Mehto et al, 2019b; Jena et al, 2020; Chauhan et al, 2021; Deretic, 2021). To date, it is unclear how selective autophagy contributes to fine-tuning of the NODs-RIPK2-NF- κ B pathways.

Genetic mutations in the Immunity-related GTPase M (IRGM) gene or promoter are suggested to increase susceptibility to several inflammatory and infectious diseases including Crohn's disease, tuberculosis, sepsis, and ankylosing spondylitis (Massey & Parkes, 2007; Parkes et al, 2007; Intemann et al, 2009; Lu et al, 2013; Kimura et al, 2014; Lin et al, 2016; Xia et al, 2017; Yao et al, 2018). IRGM is also a critical factor for antimicrobial autophagy (Singh et al, 2006; Chauhan et al, 2015). IRGM interacts with autophagy and lysosome regulatory proteins to stimulate autophagosome/lysosome biogenesis for efficient degradation of cargo including microbes (Singh et al, 2010; Chauhan et al, 2015; Kumar et al, 2018, 2020). IRGM plays a prominent role in the inflammophagy of several innate immune sensing proteins including NLRP3, RIG-I, and cGAS to limit inflammasome and interferon responses (Mehto et al, 2019a, 2019b; Jena et al, 2020; Chauhan et al, 2021; Nath et al, 2021). IRGM interacts with NOD2 to scaffold the signaling events for xenophagy (Chauhan et al, 2015); however, it is unclear whether IRGM also could regulate the activity of NODs and RIPK2 (RIPosomes) to control NF- κ B pro-inflammatory cytokine response.

Here, we demonstrate that pathogenic bacteria induce the formation of endogenous RIPosomes in the proximity of the bacteria to activate the NF- κ B cytokine response. Further, we found that NODs, RIPK2, and RIPosomes are targets of selective autophagy. The autophagy scaffolding proteins, IRGM and p62 physically interact with NODs, RIPK2, and RIPosomes, and using the canonical autophagy machinery coordinate their selective degradation to limit cytokine responses. In agreement, the global transcriptomic analysis revealed that during *Salmonella* and *Shigella* infection, IRGM suppresses multiple RIPK2-dependent pro-inflammatory pathways including NF- κ B and interferon (IFN) response. Consistently, in animal studies, inhibition of RIPK2 using GSK583 ameliorated shigellosis- and dextran sodium sulfate (DSS)-induced gut inflammation, and pathology in *Irgm1*^{KO} mice. Together, this study delineates new cell-autonomous mechanisms of NODs-RIPK2-dependent

pro-inflammatory response and its resolution by selective autophagy. Further, our study also suggests that inhibition of RIPK2 could be a good therapeutic strategy for suppression of gut inflammation associated with IRGM depletion, a risk factor in the progression of Crohn's disease.

Results

RIPosomes recruit over the bacteria

The existence of endogenous RIPK2 oligomeric structures (RIPosomes) is not reported. We found that infection of macrophage-like differentiated THP-1 cells with *Shigella flexneri* induces RIPosome formation. RIPosomes were detected only in infected cells but not in control cells (Appendix Fig S1A). Several of the RIPosomes were recruited over the bacteria (Fig 1A and Appendix Fig S1A–C and Movie EV1). However, not all the intracellular bacteria were covered with oligomeric RIPK2 puncta (Fig 1A). High-content microscopy was performed to quantitate the RIPosomes present in the cell (Fig 1B and Appendix Fig S1D). The presence of endogenous RIPK2 oligomeric structures was further confirmed by Western blotting of detergent-insoluble fractions from *Shigella*-infected cells (Fig 1C). To confirm specificity, next we depleted RIPK2 and tested the formation of RIPosomes by high-content microscopy and Western blotting. *Shigella*-induced RIPosomes were dramatically reduced upon RIPK2 siRNA knockdown in THP-1 macrophages (Fig 1D and E) or RIPK2 CRISPR knockout HT-29 cells (henceforth, RIPK2^{-/-}; Fig 1F).

Next, we infected mouse bone marrow-derived macrophages (BMDMs), HT-29 colon epithelial cells, and mouse embryonic fibroblast (MEF) cells with *Shigella*. RIPosomes were recruited over and adjacent to the bacteria in the infected cells (Fig 1G and Appendix Fig S1E–G), whereas the uninfected cells were devoid of them (Appendix Fig S1F). Thus, *Shigella* infection can induce RIPosome formation in different cell types. Next, C57BL/6 mice were infected by the intraperitoneal injection of *Shigella* (Yang et al, 2014), and immunohistochemistry with the colon tissues was performed. Several of the bacteria were covered with RIPosomes in colon tissues (Fig 1H).

To test whether RIPosome formation is specific to *Shigella* infection or is a generalized event during bacterial infection, we infected THP-1 cells with *Salmonella typhimurium*. Like *Shigella*, *Salmonella* enhanced the oligomerization of RIPK2 (Appendix Fig S1H) and triggered RIPosome formation (Fig 1I and J). Furthermore, infection with the Crohn's disease-associated adherent invasive *Escherichia coli* (AIEC) strain LF82 (Glasser et al, 2001) also prompted the formation of RIPosomes that were coating the bacteria (Fig 1K). Next, we compared RIPosome inducing capacity of pathogenic *Mycobacterium tuberculosis* (*M.tb*, H37Rv) and nonpathogenic *Mycobacterium smegmatis* (*M. smeg*, MC²155). Surprisingly, only *M.tb* triggered the massive formation of RIPosomes over the bacteria (Fig 1L and M and Appendix Fig S1I and Movie EV2), indicating that only pathogenic bacteria could activate RIPosome formation. To further corroborate this notion, we compared the RIPK2 oligomerization capacity of nonpathogenic *E. coli* DH5 α and pathogenic AIEC LF82. Indeed, LF82 was more efficient in triggering the oligomerization of RIPK2 (Fig 1N).

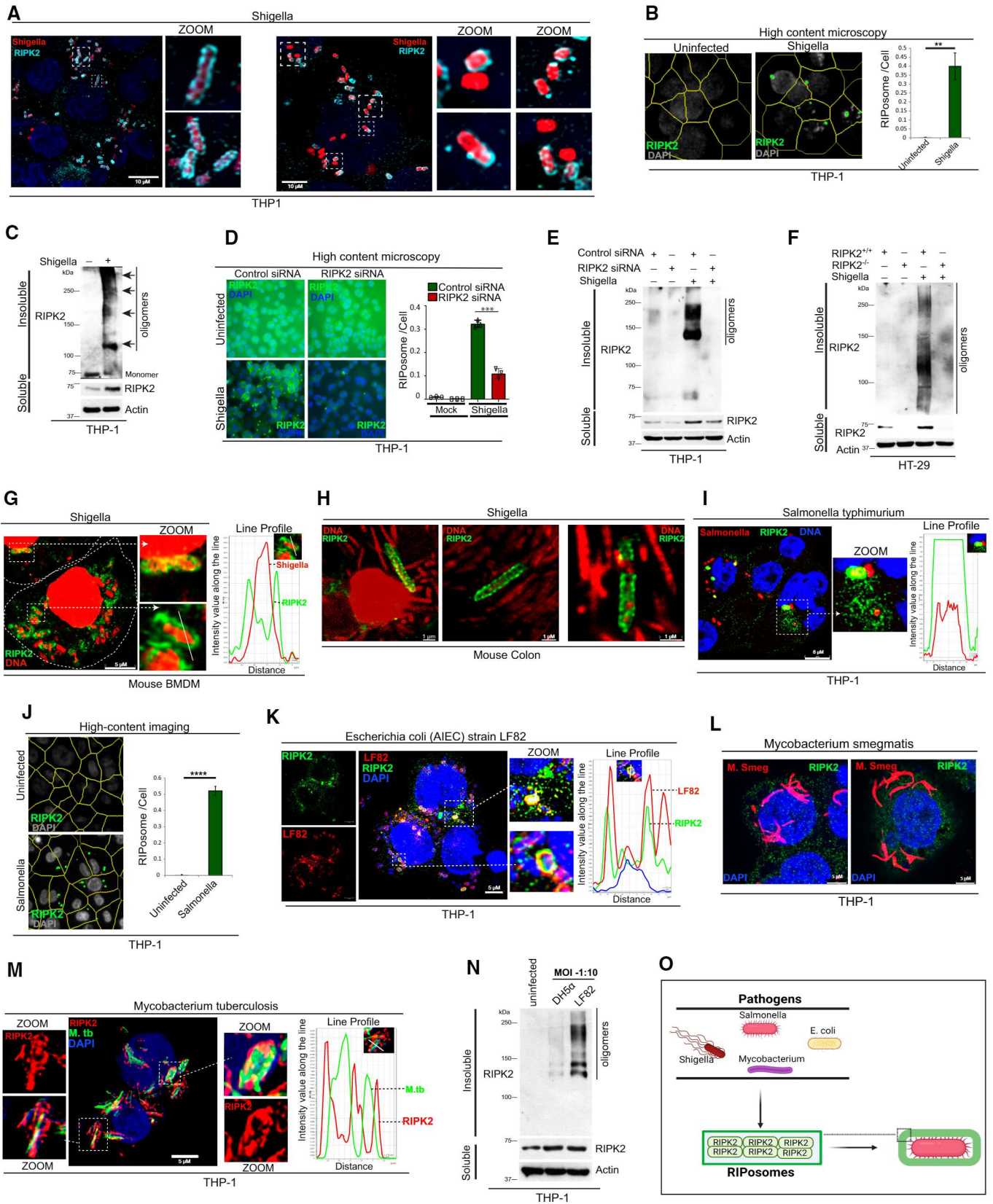


Figure 1.

Figure 1. Pathogenic bacteria trigger the formation of RIPosomes that recruit over the bacteria.

- A Representative confocal images of RIPosomes in THP-1 cells infected with a red fluorescent protein (RFP) expressing *Shigella flexneri* (MOI 1:25, 8 h). Scale bar, 10 μm . Zoom panels are digital magnifications.
- B Representative high-content microscopy images (see Appendix Fig S1D for full images; yellow masks represent software algorithms-defined cell boundaries) of RIPosomes in THP-1 cells infected with *S. flexneri* (MOI 1:25, 8 h). About 50,000 cells were plated per well and RIPosomes were screened in 35 fields per well in three technical replicates. Right panel, the graph depicts an average number of RIPosomes/cell, which is calculated from three biological replicates, Mean \pm SD. *** P < 0.005, Student's unpaired t -test.
- C Western blot analysis of soluble and insoluble fractions of *S. flexneri*-infected THP-1 cells (MOI 1:25, 8 h). Arrow indicates oligomers of RIPK2.
- D Left panel, representative high-content microscopy image of control and RIPK2 knockdown THP-1 cells infected with *S. flexneri* (MOI 1:25, 8 h). Right panel, the graph depicts an average number of RIPosomes/cell, which is calculated from three biological replicates, Mean \pm SD. **** P < 0.0005, Student's unpaired t -test.
- E, F Western blot analysis of soluble and insoluble fractions of *S. flexneri*-infected (E) control siRNA and RIPK2 siRNA transfected THP-1 cells (F) Control CRISPR (RIPK2^{+/+}) cells and RIPK2 CRISPR knockout (RIPK2^{-/-}) HT-29 cells.
- G Representative confocal images of RIPosomes in mouse BMDMs infected with *S. flexneri* (MOI 1:25, 8 h). Line profile: co-localization analysis using line intensity profile. Scale bar, 5 μm . Zoom panels are digital magnifications. DNA is stained with DAPI (pseudo-colored red for better contrast).
- H Representative confocal images of mouse colon tissues showing recruitment of RIPK2 over the *S. flexneri*. Scale bar, 1 μm . Zoom panels are super-resolution confocal images. DNA is stained with DAPI (pseudo-colored red for better contrast).
- I Representative confocal images of RIPosomes in THP-1 cells infected with RFP expressing *Salmonella typhimurium* (MOI 1:5, 4 h). Line profile: co-localization analysis using line intensity profile. Scale bar, 8 μm . Zoom panels are digital magnifications. DNA is stained with DAPI.
- J Left panel, representative high-content microscopy images (yellow masks represent software algorithms-defined cell boundaries) of RIPosomes in THP-1 cells infected with *S. typhimurium* (MOI 1:5, 4 h). The same cell numbers and conditions are used as indicated in (B). Right panel, the graph depicts an average number of RIPosomes/cell. Mean \pm SD, n = 4 (biological replicates), **** P < 0.0005, Student's unpaired t -test. DNA is stained with DAPI.
- K–M Representative confocal images of RIPosomes in THP-1 cells infected with (K) *E. coli* LF82 strain (MOI 1: 10, 8 h), (L) mCherry expressing *M. smegmatis* (MOI 1:10, 4 h) (M) mCherry (pseudocolored to green) expressing *M. tuberculosis* (MOI 1:10, 8 h). Line profile: co-localization analysis using line intensity profiles. Scale bar, 5 μm . Zoom panels are digital magnifications. DNA is stained with DAPI.
- N Western blot analysis of soluble and insoluble fractions from THP-1 cells, uninfected or infected with *E. coli* DH5 α (MOI 1:10, 8 h) or *E. coli* LF82 strains (MOI 1:10, 8 h).
- O Pictorial representation of data obtained in this figure shows that bacterial infection triggers oligomerization of RIPK2 or RIPosome formation that coats bacteria.
- Source data are available online for this figure.

No RIPosomes were formed upon infection with GFP-tagged vesicular stomatitis virus (Appendix Fig S1J). Similarly, the NOD1 and NOD2 ligands, iE-DAP or MDP were not able to trigger visible RIPosome formation (Appendix Fig S1K). However, iE-DAP or MDP increased oligomerization of RIPK2 in the insoluble fraction of cells (Appendix Fig S1L and M), suggesting that they have a reduced capacity to induce RIPK2 oligomerization.

Altogether, these findings demonstrate that bacterial infection triggers RIPosome formation that is recruited at cytoinvasive bacteria both *in vitro* and *in vivo* conditions (Fig 1O).

RIPosomes are self-assembling structures that promote NODs oligomerization

RIPK2 is a common adaptor protein for NOD1 or NOD2-dependent NF- κ B signaling. Several inflammatory proteins utilize their CARD domain to self-oligomerize and/or to hetero-oligomerize with downstream cognate signaling adaptor proteins for activation and signal transduction (Park, 2019). All three proteins, NOD1, NOD2, and RIPK2 possess CARD domain/s (Fig 2A); however, only RIPK2 self-oligomerized and formed RIPosomes (Fig 2A and B and Appendix Fig S2A) and fractionated in the insoluble (pellet) portion of cells (Appendix Fig S2B and C). Further, the CARD domain of RIPK2 (RIPK2^{CARD}) formed high-order oligomers (Fig 2C) and large filamentous structures (Fig 2D and Movie EV3), whereas the CARD domain of NOD1^{CARD} and NOD2^{CARDs} domain failed to do so (Fig 2C and D). These results suggest that only RIPK2 (but not NODs) can self-oligomerize using its CARD domain.

Interestingly, upon *Shigella* infection, endogenous NOD2 formed puncta (Appendix Fig S2D) and the oligomeric aggregates of both NOD1 and NOD2 were increased in the insoluble cell fractions (Fig 2E). NOD2 puncta were found to be juxtaposed to the bacteria

(Appendix Fig S2D) where they co-localized/juxtaposed with RIPosomes (Fig 2F and Appendix Fig S2E). This apparent discrepancy between overexpressed and endogenous results could be due to the presence of endogenous RIPK2 in THP-1 cells (compared with HEK293T) whose self-assembly may have prompted co-oligomerization of NOD1/2 leading to puncta formation. Indeed, both the NOD1 and NOD2 formed insoluble oligomeric structures when co-expressed with RIPK2, as apparent from immunofluorescence (Fig 2G and Appendix Fig S2F), quantitative high-content microscopy (Appendix Fig S2G), and soluble/insoluble fractionation assays (Fig 2H). NODs were perfectly co-localized with RIPK2 in these structures (Fig 2G and Appendix Fig S2F and G). We termed these structures NODo-RIPosomes. These data were further supported by experiments where we found NOD1^{CARD} or NOD2^{CARDs} domain/s start oligomerizing once they are co-expressed with the RIPK2^{CARD} (Fig 2I). Also, the NOD1^{CARD} or NOD2^{CARD} formed the punctate structures when co-expressed with RIPK2^{CARD} (Appendix Fig S2H and I). Taken together, the data suggest that RIPK2 facilitates the oligomerization of NOD proteins via CARD domain/s. This notion was further tested in endogenous conditions by assessing the oligomerization of NOD proteins in the absence of RIPK2. *Shigella*-induced oligomerization of endogenous NODs was reduced in RIPK2^{-/-} HT-29 cells compared with WT (Fig 2J and K). Thus, we conclude that RIPK2 self-assembling property is critical for inducing oligomerization of NOD1 and NOD2. Conversely, we noticed that the NOD proteins, in turn, enhanced the self-oligomerization capacity of RIPK2 (Appendix Fig S2J and K).

The formation of RIPosomes is important for the activation of NF- κ B signaling (Gong *et al*, 2018; Pellegrini *et al*, 2018). We used a HeLa cell line expressing stable doxycycline-inducible human GFP-RIPK2 (Ellwanger *et al*, 2019) to evaluate whether *Shigella* infection-induced RIPosomes prompt nuclear translocation of NF-

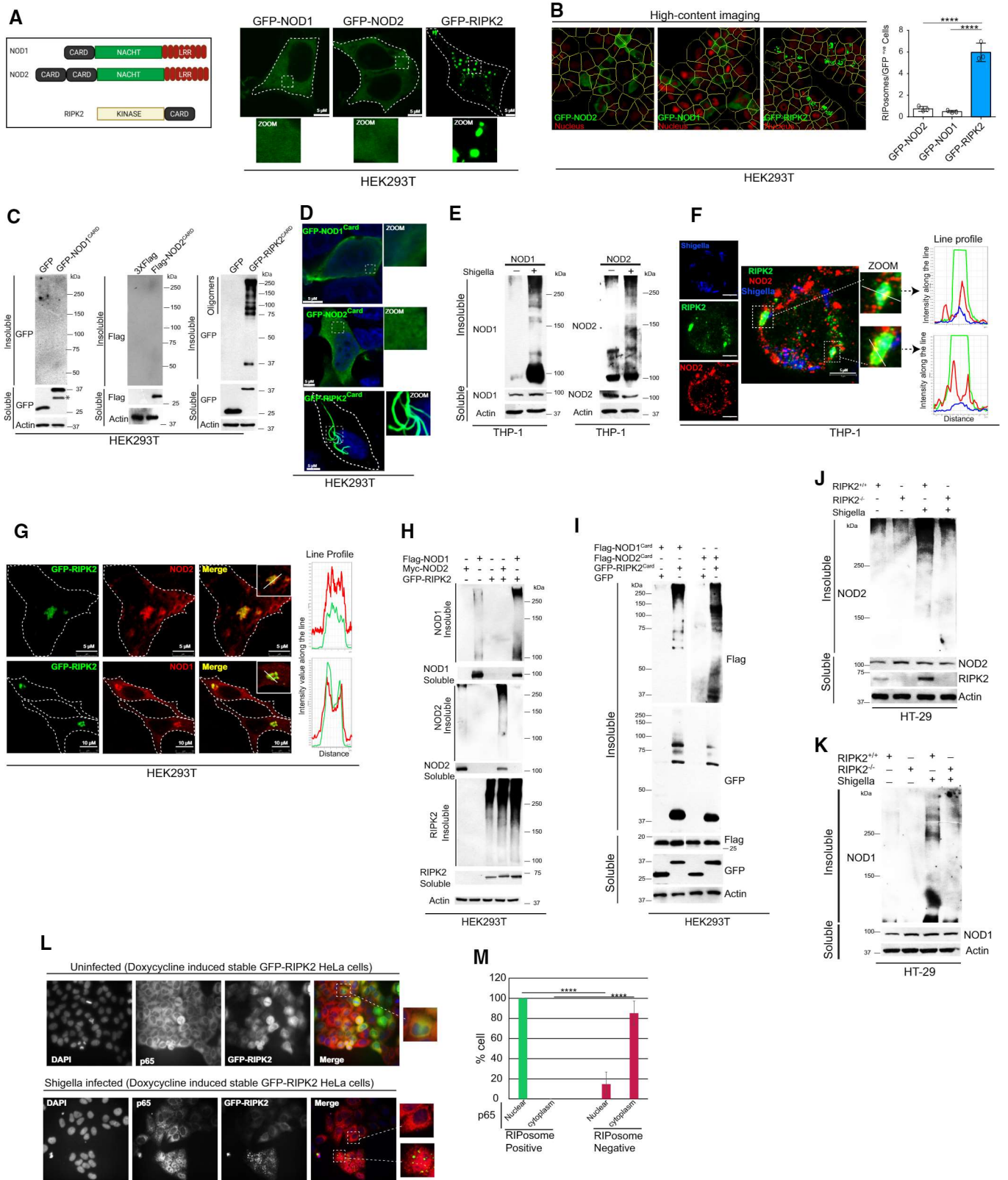


Figure 2.

Figure 2. RIPK2 oligomers provide a platform for NODs oligomerization.

- A Left panel, the domain organization map of NOD1, NOD2, and RIPK2. Right panel, representative confocal images of immunofluorescence assays performed in HEK293T cells transfected with GFP-NOD1, GFP-NOD2, and GFP-RIPK2 plasmids for 9 h. Scale bar 5 μ m.
- B Left panel, representative high-content microscopy images of HEK293T cells transfected with GFP-NOD1, GFP-NOD2, and GFP-RIPK2 plasmids for 9 h. Right panel, the graph depicts the average number of RIPosomes per GFP-positive cell. About 15,000 cells were plated per well and RIPosomes were screened in 35 fields per well. Mean \pm SD, $n = 3$ (biological replicates), **** $P < 0.00005$, ordinary one-way ANOVA (Tukey's multiple comparisons test).
- C Western blot analysis of soluble and insoluble fractions of HEK293T cells transfected with the CARD domain-containing region of NOD1, NOD2, and RIPK2.
- D Representative confocal images of HEK293T cells transfected with GFP-NOD1^{CARD}, GFP-NOD2^{CARD}, and GFP-RIPK2^{CARD}. Scale bar 5 μ m.
- E The soluble and insoluble fractions of *S. flexneri*-infected THP-1 (MOI 1:25, 8 h) cell lysates were subjected to Western blot analysis with indicated antibodies.
- F Representative confocal images of immunofluorescence assays conducted with THP-1 cells infected with RFP expressing *S. flexneri* (pseudo-colored, blue) (MOI 1:25, 8 h). Line profile: co-localization analysis using line intensity profiles. Scale bar, 5 μ m. Zoom panels are digital magnifications.
- G Representative confocal images of immunofluorescence assays performed with HEK293T cells transfected with GFP-RIPK2 and Flag-NOD2 (upper panel) or Flag-NOD1 (lower panel). Line profile: co-localization analysis using line intensity profiles. Scale bar, 5 or 10 μ m as indicated in figures. Inset zoom panels are digital magnifications.
- H, I HEK293T cells were transfected with (H) full length and (I) CARD domains of NOD1, NOD2, and RIPK2 followed by Western blot analysis with soluble and insoluble fractions using indicated antibodies.
- J, K Western blot analysis of soluble and insoluble fractions of RIPK2^{+/+} and RIPK2^{-/-} HT-29 cells infected with *S. flexneri* (MOI 1:25, 8 h) with indicated antibodies.
- L, M Representative immunofluorescence images of doxycycline-inducible GFP-RIPK2 expressing HeLa cells. (L) Upper panel, uninfected. Lower panel, *S. flexneri*-infected (MOI 1:25, 4 h). Immunostaining was performed with the p65 antibody (red) and DNA stained with DAPI (Blue). (M) The graph indicates % of cells that are RIPosomes positive or negative with nuclear/cytoplasmic p65 (5 fields (each group), Mean \pm SD, $n = 3$). **** $P < 0.00005$, Student's unpaired *t*-test.

Source data are available online for this figure.

κ B-p65, a signature of NF- κ B activation. The p65 was not translocated into the nucleus in uninfected GFP-RIPK2 expressing cells (Fig 2L, upper panel), whereas a distinct nuclear translocation was observed in the *Shigella*-infected cells in which the RIPosomes are formed (Fig 2L, lower panel and M). However, within the *Shigella*-infected cells, the cells that are negative for RIPosomes, a majority had cytoplasmic p65 (Fig 2L, lower panel and M). Also, the nuclear translocation of phospho-p65 (Ser536) is significantly induced upon *Shigella* infection in GFP-RIPK2 overexpressing HeLa cells (Appendix Fig S2L). The data suggest that the biogenesis of RIPosome is important for the activation of NF- κ B response.

To evaluate whether the NODo-RIPosomes could also induce NF- κ B activation, we electroporated purified RIPosomes and NODo-RIPosomes into HEK293T cells. Both RIPosomes and NODo-RIPosomes induced NF- κ B activation measured by luciferase reporter assays, where NODo-RIPosomes were consistently more efficient than RIPosomes in triggering NF- κ B activation (Appendix Fig S2M).

NODs, RIPK2, and RIPosomes are the target of selective autophagy

We performed cycloheximide chase assays to determine the role of proteasome and/or autophagy processes in the turnover of endogenous NODs and RIPK2. The inhibition of autophagy flux using Bafilomycin A1 (Baf A1) completely protected RIPK2 and NOD1 from degradation, whereas proteasome inhibition using MG132 was partially protective (Fig EV1A and B). In the case of NOD2, only inhibition of autophagy protected it from degradation (Fig EV1C). These data indicate that autophagy plays a major role in the degradation of NODs and RIPK2. To confirm the role of autophagy in NODs and RIPK2 degradation, we monitored the levels of these proteins in ATG5 knockdown THP-1 or ATG5 knockout MEFs cells in uninfected and *Shigella*-infected cells. Enhanced amounts of RIPK2, NOD1, and NOD2 were detected in the ATG5-depleted cells both in control or *Shigella*-infected cells confirming that autophagy is critical in suppressing the levels of NODs and RIPK2 (Fig 3A and B).

Next, we tested whether RIPosomes are the target of autophagy. Treatment of cells with rapamycin dramatically reduced the number

of RIPosomes (Fig 3C). This effect was completely rescued when the cells were additionally treated with Baf A1 (Fig 3C). Further, the numbers of RIPosome were significantly increased in the absence of ATG5 in *Shigella*-infected THP-1 cells (Fig 3D). Additionally, although RIPK2 soluble levels were induced in ATG5-depleted cells in basal conditions, RIPosomes (insoluble oligomeric aggregates) were formed only as a result of *Shigella* infection and were further induced in ATG5 KD cells (Fig 3E). Collectively, these results demonstrate that NODs and RIPK2 proteins as well as RIPosomes are the targets of autophagy.

SQSTM1/p62 mediates selective autophagy of ubiquitinated RIPosomes

Ubiquitin marks cargoes before the autophagy machinery recognizes them and degrades them (Shaid *et al*, 2013). The infection of *Shigella* induced the K63-linked ubiquitination of RIPK2 (Fig EV1D). An evident co-localization or juxtaposition of ubiquitin with RIPosomes was observed in HEK293T cells (Fig 3F) and *Shigella*-infected THP-1 cells (Fig EV1E). To understand whether ubiquitination of RIPosomes is important for their autophagic degradation, we inhibited ubiquitination in cells using PYR-41, which is a selective and cell-permeable inhibitor of ubiquitin-activating enzyme E1. In high-content microscopy, we found that rapamycin-induced autophagic degradation of RIPosomes is blocked by PYR-41 (Fig EV1F), indicating that ubiquitinated RIPosomes are the target of autophagy.

Autophagy receptor proteins are critical in bridging the ubiquitinated cargoes to the autophagosomes (Shaid *et al*, 2013). To identify the receptor that recognizes RIPK2, we screened the interaction between RIPK2 and key autophagy receptors, including p62, NBR1, NDP52, TAX1BP1, and Optineurin (Fig 3G). A strong physical interaction was observed between RIPK2 and p62 (Fig 3G). NBR1 was faintly bound and other receptors completely failed to interact with RIPK2 (Fig 3G). Thus, we tested whether p62 mediates autophagic degradation of RIPK2 and RIPosomes. Levels of both soluble and insoluble forms of RIPK2 were increased in *Shigella*-infected THP-1 cells upon p62 knockdown (Fig 3H). Also, we found an increased number of RIPosomes in p62 knockdown cells compared with

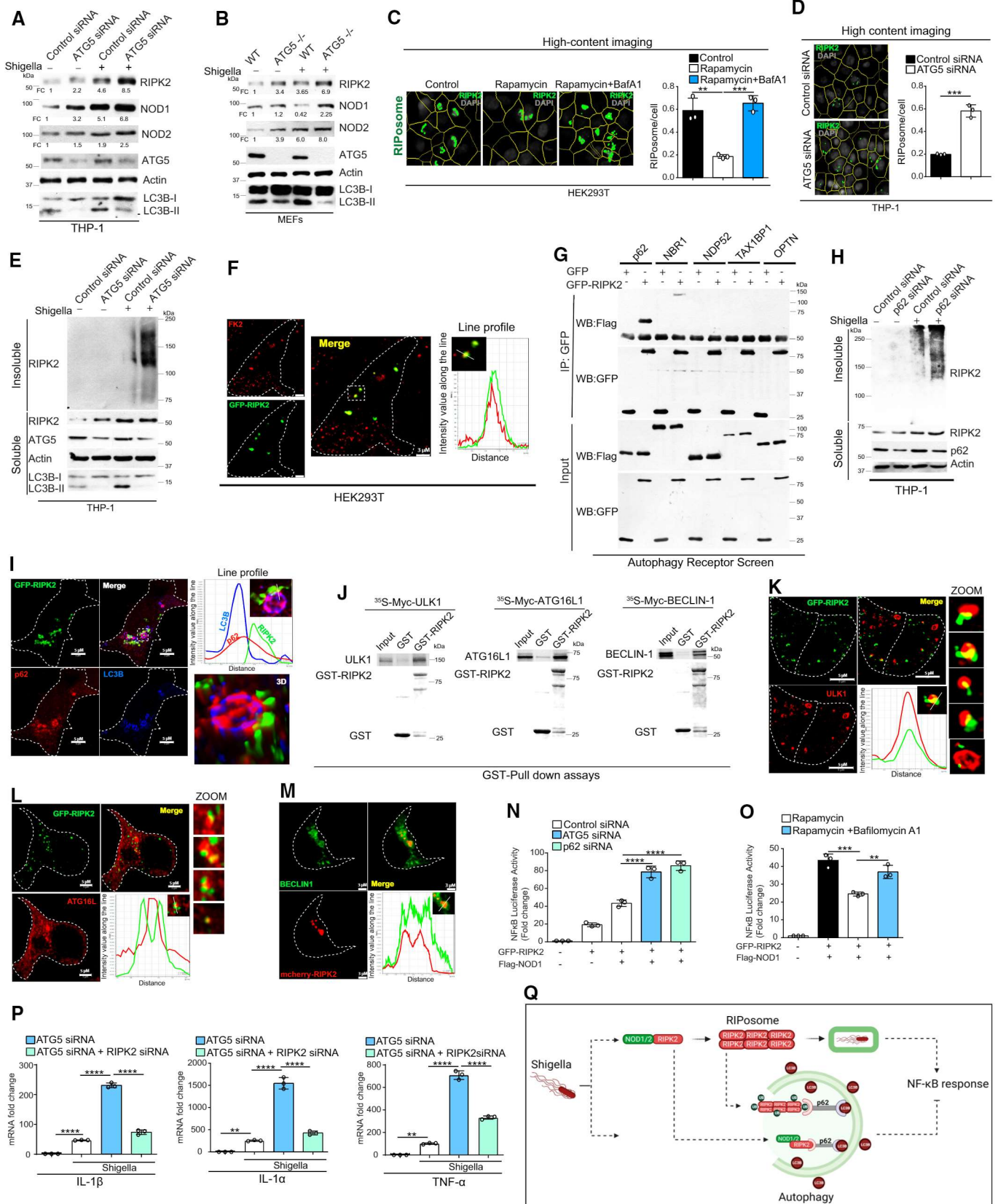


Figure 3.

Figure 3. NODs, RIPK2, and RIPosomes are degraded by p62-dependent selective autophagy.

- A, B Western blot analysis with cell lysate of uninfected and *S. flexneri*-infected (MOI 1:25, 8 h) (A) control and ATG5 siRNA knockdown THP-1 cells, (B) wild-type (WT) and ATG5 knockout (ATG5^{-/-}) MEF cells with indicated antibodies. Densitometric analysis was performed using Image J software. FC, fold change.
- C Left panel, representative high-content microscopy images of RIPosomes in HEK293T cells that are control cells or cells treated with rapamycin (500 nM, 4 h) or cells treated with rapamycin (500 nM, 4 h) and bafilomycin A1 (BafA1, 300 nM). Right panel, the graph depicts the average number of RIPosomes/cell. About 15,000 cells were plated per well and RIPosomes were screened in 35 fields per well. Mean \pm SD, $n = 3$ (biological replicates), ** $P < 0.005$ and, *** $P < 0.0005$, ordinary one-way ANOVA (Tukey's multiple comparisons test).
- D Left panel, representative high-content microscopy images of RIPosomes in control and ATG5 siRNA transfected THP-1 cells infected with *S. flexneri* (8 h). Right panel, the graph depicts average number of RIPosomes/cell. About 50,000 cells were plated per well and RIPosomes were screened in 35 fields per well. Mean \pm SD, $n = 3$ (biological replicates), *** $P < 0.0005$, Student's unpaired t -test.
- E The soluble and insoluble fractions of *S. flexneri*-infected (MOI 1:25, 8 h) control and ATG5 siRNA knockdown THP-1 cells were subjected to Western blot analysis with indicated antibodies.
- F Representative confocal images of HEK293T cells transfected with GFP-RIPK2 and immunostained with anti-FK2 antibodies. Line profile: co-localization analysis using line intensity profiles. Scale bar, 3 μ m.
- G Autophagy receptor screen using co-immunoprecipitation (Co-IP) assay to analyze the interaction between GFP-RIPK2 and Flag-p62 or Flag-NBRI or Flag-NDP52 or Flag-TAX1BP1 or Flag-OPTINEURIN in HEK293T cell lysate.
- H Western blot analysis of soluble and insoluble fractions of control and p62 siRNA transfected and *S. flexneri*-infected THP-1 cells (MOI 1:25, 8 h).
- I Representative confocal images of HEK293T cells expressing GFP-RIPK2 (6 h) immunostained with p62 and LC3B antibodies. Zoom panels are digital magnifications.
- J GST pull-down assay using purified GST or GST-RIPK2 proteins with in vitro translated ³⁵S radiolabeled myc-ULK1 or myc-ATG16L or myc-BECLIN1.
- K–M Representative confocal images of HEK293T cells transfected with GFP-RIPK2 or mcherry-RIPK2 (9 h) and immunofluorescence assay performed with antibodies specific to (K) ULK1, (L) ATG16L (M) BECLIN1. Line profile: co-localization analysis using line intensity profiles. Scale bar, 5 or 3 μ m as indicated. Zoom panels are digital magnifications.
- N Luciferase assays were performed with ATG5 or p62 knockdown HEK293T cells transfected with NF- κ B luciferase reporter vector pGL4.32 NF κ B-RE, GFP-RIPK2, and Flag-NOD1 plasmids. Mean \pm SD, $n = 3$ (biological replicates), **** $P < 0.00005$, ordinary one-way ANOVA (Tukey's multiple comparisons test).
- O Luciferase assays performed with HEK293T cells transfected with NF- κ B luciferase reporter vector pGL4.32NF κ B-RE, GFP-RIPK2, and Flag-NOD1 plasmids followed by treatment with rapamycin (500 nM, 4 h) alone or in combination with bafilomycin A1 (300 nM, 5 h). Mean \pm SD, $n = 3$ (biological replicates), ** $P < 0.005$ and *** $P < 0.0005$, ordinary one-way ANOVA (Tukey's multiple comparisons test). The control conditions and readings for Fig 3N and P are the same.
- P The qRT-PCR analysis with total RNA isolated from the uninfected and *S. flexneri*-infected (MOI 1:25, 6 h) control or ATG5 knockdown or ATG5 and RIPK2 double knockdown THP-1 cells. Mean \pm SD, $n = 3$ (biological replicates), ** $P < 0.005$, and **** $P < 0.00005$, ordinary one-way ANOVA (Tukey's multiple comparisons test).
- Q Pictorial representation of results obtained in this section where we found that p62-dependent selective autophagy degrades NODs, RIPK2, and RIPosomes to suppress NF- κ B cytokine response.

Source data are available online for this figure.

control cells (Fig EV1G), suggesting that p62 plays a critical role in the autophagic degradation of RIPosomes. In agreement, p62 and LC3B (autophagosomes) were either co-localized or juxtaposed to RIPosomes (Figs 3I and EV1H). The high-resolution microscopy and 3D rendering of images indicate that p62 tethered the RIPosome to LC3B decorated autophagosomes (Fig 3I). Also, LC3B was found to be co-localized with RIPosome recruited over the *Shigella* (Fig EV1I).

Next, we asked whether other key autophagosome initiations (ULK1) and elongation proteins (ATG16L1 and BECLIN1) interact and co-localize with RIPK2/RIPosomes. We found that *in vitro* translated ULK1, BECLIN1, and ATG16L1 directly interacted with purified GST-RIPK2 in GST pull-down assays (Fig 3J). Further, all the three important autophagy proteins were either completely co-localized or juxtaposed to the RIPosomes (Figs 3K–M and EV1J and K) indicating a *de novo* biogenesis of autophagosomes occurring adjacent to the RIPosomes for their degradation. When cargo is degraded via autophagy, typically autophagy receptors specifically p62 also subjected to degradation. We observed that p62 is degraded upon *Shigella* infection and this degradation is rescued upon Bafilomycin A1 treatment, suggesting that p62 is targeted by autophagy along with cargo upon *Shigella* infection (Fig EV1L).

The depletion of ATG5 and p62 significantly increased NOD1/RIPK2-dependent NF- κ B activity in luciferase reporter assays (Fig 3N). Conversely, autophagy activation by rapamycin reduced the NOD1/RIPK2-dependent NF- κ B activity (Fig 3O) that was rescued by Baf A1 treatment (Fig 3O). Finally, the depletion of ATG5 or p62 significantly enhanced *Shigella*-induced NF- κ B-mediated pro-inflammatory cytokine response (TNF α , IL-1 β , and IL-1 α) in THP-1

cells (Figs 3P and EV1M). This enhanced cytokine response was rescued by RIPK2 silencing (Figs 3P and EV1M), suggesting that autophagy suppresses RIPK2-dependent NF- κ B pro-inflammatory cytokine response.

Altogether, we found that p62-dependent selective autophagy mediates the degradation of NODs, RIPK2, and RIPosomes to suppress NF- κ B activation and pro-inflammatory cytokine response (Fig 3Q).

Autophagy protein, IRGM is recruited over the bacteria and interacts with RIPosomes

IRGM is an autophagy protein that plays a critical role in the selective autophagic degradation of pro-inflammatory proteins (Mehto et al, 2019a, 2019b; Jena et al, 2020; Chauhan et al, 2021). We set out to examine the role of IRGM in the autophagic degradation of NODs, RIPK2, and RIPosomes. For that, first, we tested whether IRGM interacts with NODs and RIPK2. In the immunoprecipitation (IP) assays, endogenous IRGM interacted with RIPK2 and NODs (Fig 4A and B). The interaction of IRGM with NOD1/RIPK2 and NOD2/RIPK2 complex is further increased when the cells were treated with iE-DAP (NOD1 agonist) or MDP (NOD2 agonist), respectively (Fig 4A and B). In IP assays with the HT-29 cell line stably expressing Flag-IRGM, IRGM immunoprecipitated endogenous NOD1, NOD2, and RIPK2 (Appendix Fig S3A). A strong interaction between overexpressed IRGM with NOD1, NOD2, and RIPK2 was also observed in HEK293T cells (Fig 4C and D, and Appendix Fig S3B). Furthermore, a direct interaction of purified

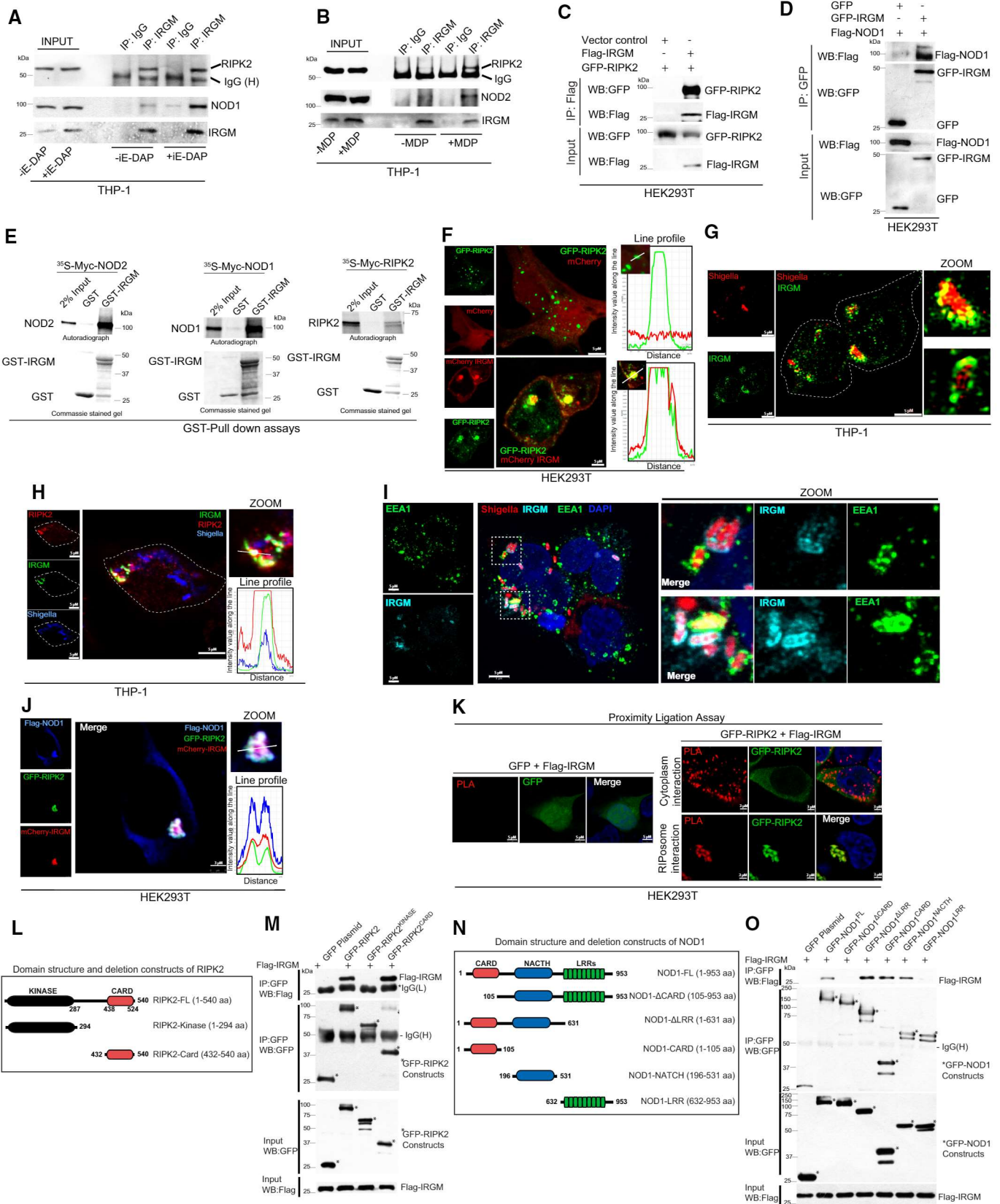


Figure 4.

Figure 4. Autophagy protein IRGM interacts and co-localizes with NODs, RIPK2, and RIPosomes.

- A, B The THP-1 cell lysates were subjected to immunoprecipitation analysis (A) untreated and treated with iE-DAP (40 $\mu\text{g}/\text{ml}$, 6 h), (B) untreated and treated with MDP (40 $\mu\text{g}/\text{ml}$, 6 h). IP was performed with isotype control IgG or IRGM antibody and Western blotting was performed with indicated antibodies. IgG (H), IgG heavy chain.
- C, D Co-IP analysis of the interactions between (C) GFP-RIPK2 and Flag-IRGM or (D) Flag-NOD1 and GFP-IRGM in HEK293T cell lysates.
- E GST pull-down assay using purified GST and GST-IRGM and *in vitro* translated ^{35}S radiolabeled myc-NOD2, myc-NOD1, and myc-RIPK2.
- F Representative confocal images of HEK293T cells expressing GFP-RIPK2 and mCherry or mCherry-IRGM. Line profile: co-localization analysis using line intensity profiles. Scale bar, 5 μm .
- G, H Representative confocal images of THP-1 cells infected with RFP expressing *S. flexneri*, (MOI 1:25, 8 h) and immunostained with, (G) IRGM antibody (H) IRGM and RIPK2 antibody. Line profile: co-localization analysis using line intensity profiles. Scale bar, 5 μm . Zoom panels are digital magnifications. In image (H) for better contrast, RFP expressing *Shigella* is pseudo-colored to blue.
- I Representative confocal images of THP-1 cells infected with RFP expressing *S. flexneri*, (MOI 1:25, 20 min) and immunostained with IRGM and EEA1 antibodies. DNA stained with DAPI. Scale bar, 5 μm . Zoom panels are digital magnifications.
- J Representative confocal images of HEK293T cells expressing GFP-RIPK2, Flag-NOD1, and mCherry-IRGM. Line profile: co-localization analysis using line intensity profiles. Scale bar, 3 μm . Zoom panels are digital magnifications.
- K Representative confocal images of proximity ligation assay (PLA) in HEK293T transfected with GFP or GFP-RIPK2 and Flag-IRGM plasmid. Scale bar 3 or 5 μm as indicated.
- L The domain organization map of RIPK2 and deletion construct cloned as GFP-tagged proteins.
- M A co-IP analysis is performed with HEK293T cell lysates expressing various domains of RIPK2 and IRGM to map the domain/s of RIPK2 interacting with IRGM. Asterisk indicates the main band of overexpressed protein.
- N The domain organization map of NOD1 and deletion construct cloned as GFP-tagged proteins.
- O A co-IP analysis is performed with HEK293T cell lysates expressing various domains of NOD1 and IRGM to map the domain/s of NOD1 interacting with IRGM. Asterisk indicates the main band of overexpressed protein.

Source data are available online for this figure.

GST-IRGM with NODs and RIPK2 was observed in GST pull-down assays (Fig 4E).

IRGM does not form oligomeric structures alone in the cells (Appendix Fig S3C). However, when expressed together with RIPK2, IRGM formed structures that were fully co-localized or juxtaposed to RIPosomes (Fig 4F and Appendix Fig S3D). Analysis of data from quantitative high-content microscopy displayed a high level of co-localization between IRGM and RIPK2 (Appendix Fig S3E). Interestingly, in *Shigella*-infected cells, IRGM was recruited to the intracellular bacteria (Fig 4G and Movie EV4) together with RIPosomes (Fig 4H). In some cells, we observed the formation of cage-like structures of RIPK2 and IRGM surrounding the bacteria (Appendix Fig S3F). *Shigella* is a predominantly cytosolic bacterium that ruptures its bacteria-containing vesicle very rapidly (within 10–15 min) after the invasion (Ray *et al*, 2010; Lopez-Montero & Enninga, 2018). Also, *Shigella* tends to avoid the recruitment of Rab GTPases and other maturation proteins (including LAMP proteins) using several mechanisms (Ray *et al*, 2010; Lopez-Montero & Enninga, 2018). We infected THP-1 cells with *Shigella* for 20 min and performed immunofluorescence with EEA1 (early phagosome/endosome marker) or LAMP2A (late phagosome maturation marker) and IRGM to understand whether IRGM is recruited to phagosomal or cytosolic *Shigella*. We found that very few bacteria were positive for EEA1 protein (Fig 4I) and did not observe LAMP2A recruitment over the *Shigella* (Appendix Fig S3G) confirming the previous observations. EEA1-marked phagosomes were rarely localized with IRGM, whereas IRGM was recruited to several of the bacteria. The data suggest that IRGM is recruited to *Shigella* once they escape phagosomes and are in the cytosolic compartment. Also, IRGM was found to be recruited on NOD-RIPosome complexes (Fig 4J and Appendix Fig S3H). IRGM and RIPK2 interaction was confirmed by proximity ligation assay (PLA), which reports direct protein–protein interactions (Fig 4K). Direct interaction between IRGM and RIPK2 was observed in the cytosol as well as over the RIPosomes (Fig 4K).

NOD2 interacts with IRGM primarily via CARD domain (Chauhan *et al*, 2015). We mapped the domain by which RIPK2 or NOD1 interact with IRGM. RIPK2 has one kinase and one CARD domain (Fig 4L), but only the CARD domain interacted with IRGM (Fig 4M). NOD1 consists of a CARD, a NACTH, and several LRR domains (Fig 4N). The CARD and NACTH domains are utilized by NOD1 to interact with IRGM (Fig 4O, lanes 5 and 6). No interaction was detected with the LRR domain (Fig 4O, lane 7). Consistently, deleting LRR domains did not affect the NOD1-IRGM interaction (or rather increased interaction; Fig 4O, lane 4); however, removing the CARD domain abolished NOD1-IRGM interaction (Fig 4O, lane 3), suggesting that the CARD domain may provide a primary interface for the interaction (Fig 4O, lane 3). Thus, the findings suggest that the CARD domain of NODs and RIPK2 provides a primary interface for interaction with IRGM.

In summary, IRGM strongly and specifically interacts with NODs and RIPK2. We show that IRGM is recruited to the cytosolic *Shigella* bacteria where it co-localizes with RIPosomes. Along with IRGM, other autophagy proteins including ULK1 and p62 were recruited to the *Shigella* bacteria (Appendix Fig S3I and J). ULK1 which is a known interaction partner of IRGM (Chauhan *et al*, 2015) was found to be completely covering the bacteria along with IRGM (Appendix Fig S3J).

IRGM mediates NODs, RIPK2, and RIPosome degradation to suppress NF- κ B response

Next, we investigated how IRGM interaction with NODs, RIPK2, and RIPosomes modulates their functions. An increased protein level of RIPK2 and NODs was observed in IRGM CRISPR (partial) knockout HT-29 (IRGM^{+/-}) cells compared with the control cells (Fig 5A). The IRGM^{+/-} HT29 cells are described previously (Jena *et al*, 2020). Also, *Shigella*-induced expression of NODs and RIPK2 was further enhanced in IRGM^{+/-} HT-29 cells (Fig EV2A). Increased protein levels of NODs and RIPK2 were detected in colons and BMDMs of *Irgm1* knockout

(*Irgm1*^{-/-}) mice (Fig 5B). An increased amount of insoluble oligomeric RIPK2 was observed in *Irgm1*^{-/-} BMDMs lysates as compared to the control cells (Fig 5B). Next, we used a HeLa cell line expressing stable doxycycline-inducible human GFP-RIPK2 (Ellwanger et al, 2019). Silencing IRGM in the *Shigella*-infected cells enhanced the levels of NODs and RIPK2 (Fig EV2B), and a significantly increased number of RIPosomes was observed (Fig 5C). Conversely, transient and stable overexpression of IRGM in HT-29, THP-1, and HEK293T cells resulted in degradation of endogenous and

overexpressed NODs and RIPK2 (Figs 5D and E, and EV2C-E). Overexpression of IRGM significantly reduced the RIPosomes and NODo-RIPosomes formed in the cells (Figs 5F and EV2F). Also, the expression of IRGM reduced the insoluble oligomeric forms of RIPK2 and NOD2/RIPK2 (Figs 5G and EV2G). IRGM was found to be co-localized with RIPK2^{CARD} and was able to degrade the RIPK2^{CARD} filamentous structure into small punctate assemblies (Figs 5H, and EV2H and I). Taken together, the data show that IRGM mediates the degradation of NODs, RIPK2, and RIPosomes.

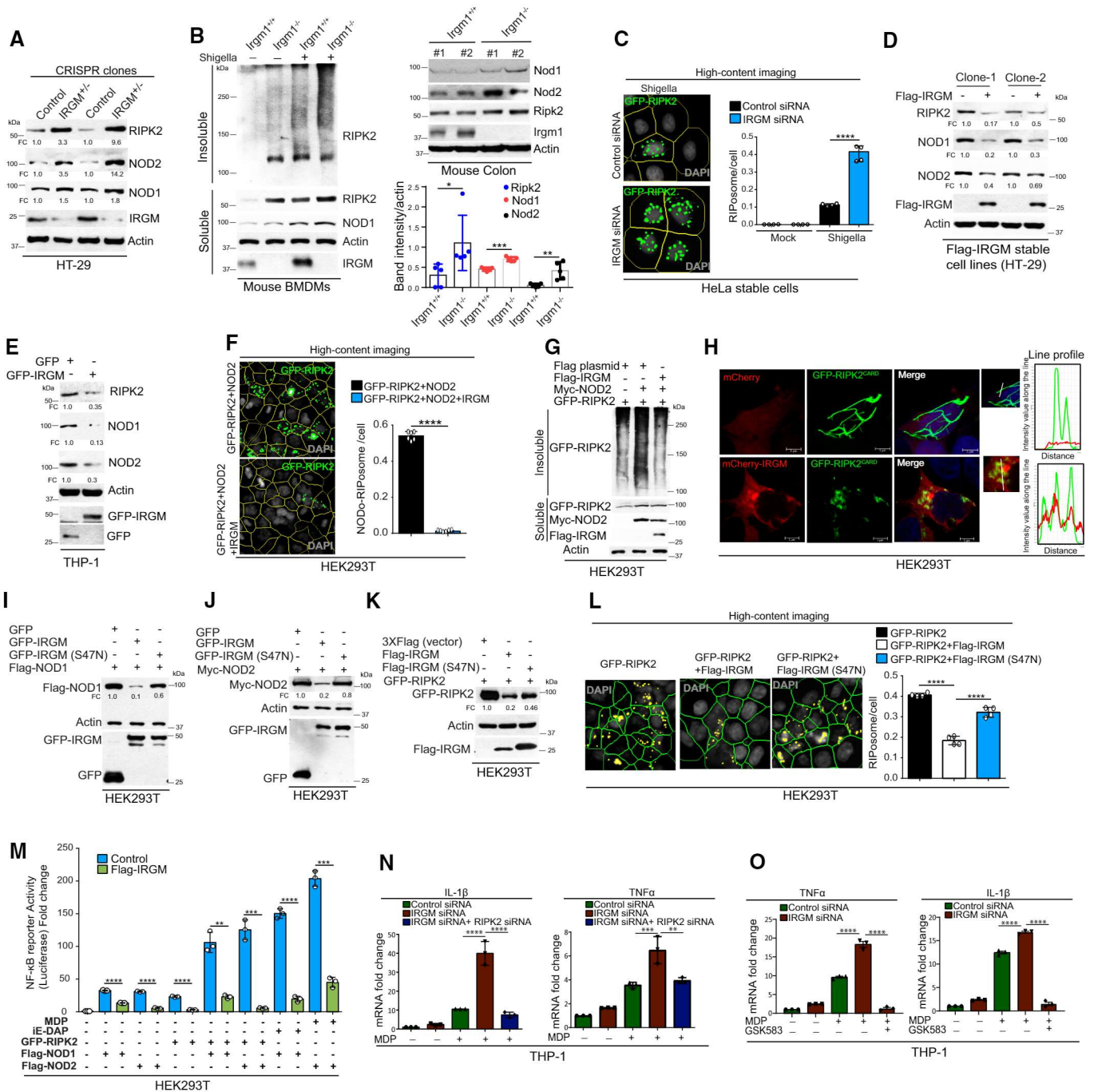


Figure 5.

Figure 5. IRGM mediates the degradation of NODs, RIPK2, and RIPosomes to suppress NF- κ B-dependent cytokine response.

- A Western blot analysis with the cell lysates of control CRISPR cells and CRISPR-Cas9 mediated IRGM partial knockout (IRGM^{+/-}) HT-29 cells (2 clones were tested). Densitometric analysis was performed using Image J software. FC, fold change.
- B Left panel, soluble and insoluble fractions of *S. flexneri* (MOI 1:25, 8 h) infected mouse BMDMs from *Irgm1*^{+/+} and *Irgm1*^{-/-} mice were subjected to immunoblot analysis with antibodies as indicated. Right panel, Western blot analysis with the colon lysates from *Irgm1*^{+/+} and *Irgm1*^{-/-} mice with indicated antibodies. The graph indicate ratio of band intensity (measured using ImageJ) and actin ($n = 5$, Mean \pm SD, * $P < 0.05$, ** $P < 0.005$, and **** $P < 0.00005$, Student's unpaired t -test).
- C Doxycycline-inducible stable GFP-RIPK2 HeLa cells were transfected with control siRNA or IRGM siRNA followed by infection with *S. flexneri* (MOI 1:25, 4 h). The cells were fixed and subjected to high-content microscopy to quantitate the number of RIPosomes formed. The graph depicts an average number of RIPosome/cell. About 10,000 cells were plated per well and RIPosomes were screened in 35 fields per well. Mean \pm SD, $n = 4$ (biological replicates), **** $P < 0.00005$, Student's unpaired t -test.
- D, E Western blot analysis with the cell lysate of (D) HT-29 clones stably expressing Flag-vector control or Flag-IRGM (E) THP-1 cells transiently transfected with GFP or GFP-IRGM for 6 h. Densitometric analysis was performed using Image J software. FC, fold change.
- F Left panel, representative high-content microscopy images of NODo-RIPosomes in HEK293T cells transfected with GFP-RIPK2 and myc-NOD2 (upper panel) or GFP-RIPK2, myc-NOD2, and Flag-IRGM (lower panel). Right panel, the graph depicts average number of NODo-RIPosome/cell. About 15,000 cells plated per well and RIPosomes were screened in 35 fields per well. Mean \pm SD, $n = 5$ (biological replicates), **** $P < 0.00005$, Student's unpaired t -test.
- G The soluble and insoluble fractions of HEK293T cells transfected with indicated plasmids were subjected to immunoblot analysis with indicated antibodies.
- H Representative confocal images of HEK293T cells transfected with mCherry and GFP-RIPK2^{CARD} or mCherry-IRGM and GFP-RIPK2^{CARD} for 9 h. Line profile: colocalization analysis using line intensity profiles. Scale bar, 5 μ m.
- I-K Western blot analysis with the cell lysates of HEK293T transfected with indicated plasmids and probe with Actin, Flag, Myc, and, GFP antibodies as indicated. Densitometric analysis was performed using Image J software. FC, fold change.
- L Left panels, representative high-content microscopy images of HEK293T cells transfected with GFP-RIPK2 or GFP-RIPK2 and Flag-IRGM or GFP-RIPK2 and Flag-IRGM (S47N). The graph depicts the average number of RIPosome/cell. The details are mentioned in the legends of Fig 1F. Mean \pm SD, $n = 4$ (biological replicates), **** $P < 0.00005$, ordinary one-way ANOVA (Tukey's multiple comparisons test).
- M Luciferase assays performed with HEK293T cells transfected with NF- κ B luciferase reporter vector pGL4.32NF κ B-RE, along with plasmids as indicated, followed by treatment with MDP (10 μ g/ml, 4 h) or iE-DAP (10 μ g/ml, 4 h) as indicated. Mean \pm SD, $n = 3$ (biological replicates), ** $P < 0.005$, *** $P < 0.0005$ and **** $P < 0.00005$, Student's unpaired t -test.
- N, O The qRT-PCR analysis with total RNA isolated from THP1 cells transfected with indicated siRNA and treated with (N) L-18 MDP (1 μ g/ml, 6 h) for indicated genes (O) L-18 MDP (1 μ g/ml, 6 h) and GSK583 (1 μ M). Mean \pm SD, $n = 3$ (biological replicates), * $P < 0.05$, ** $P < 0.005$, *** $P < 0.0005$ and, **** $P < 0.00005$, ordinary one-way ANOVA (Tukey's multiple comparisons test).

Source data are available online for this figure.

A point mutation in the GTPase domain (Serine to Glycine at 47th position, S47N) of IRGM renders it inactive to perform autophagy functions (Chauhan *et al.*, 2015; Kumar *et al.*, 2018; Mehto *et al.*, 2019a; Jena *et al.*, 2020). As compared to wild-type IRGM, the catalytic mutant (S47N) of IRGM was unable to mediate the degradation of NOD1 (Fig 5I), NOD2 (Fig 5J), RIPK2 (Fig 5K), RIPK2^{CARD} (Fig EV2J), and their oligomers (Figs 5L and EV2K). These results demonstrate the specificity of IRGM-mediated effects and also indicate the role of GTPase-dependent autophagy activity of IRGM in the degradation of NODs, RIPK2, and their oligomers.

Next, we examined the effect of IRGM on NODs/RIPK2-dependent NF- κ B activation. First, we chased the phosphorylation (Ser536) status of p65 (p-p65) in the presence and absence of IRGM. The p-p65 is induced upon *Shigella* infection that is further increased upon IRGM knockdown (Appendix Fig S4A). The data suggest that *Shigella*-induced IRGM expression suppresses the NF- κ B activation. In luciferase NF- κ B reporter assays, IRGM strongly suppressed basal and NODs agonists (MDP and iE-DAP) induced NF- κ B promoter activity (Fig 5M). We also employed an MDP-inducible NOD2 expressing secreted alkaline phosphatase (SEAP)-based NF- κ B reporter cell line (Invivogen) to assess the effect of IRGM on NF- κ B response. The overexpression of IRGM diminished MDP-induced NOD2 and NOD2-RIPK2 dependent NF- κ B reporter activity (Fig EV2L). By contrast, silencing IRGM in MDP-treated THP-1 cells resulted in increased mRNA expression of IL-1 β and TNF α (Fig 5N), which was restored in the RIPK2-depleted cells (Fig 5N). Similarly, GSK583, a specific and potent inhibitor of RIPK2 (Haile *et al.*, 2016), suppressed the cytokine response increased upon IRGM knockdown (Fig 5O). Taken together, our results show

that IRGM facilitates the degradation of NODs, RIPK2, and their oligomers to suppress NF- κ B activity and cytokine response.

Endogenous IRGM levels in cells were increased upon exposure to *Shigella*, (Figs 5B, and EV2A and B; compare lanes 1 and 3), MDP (Appendix Fig S4B and D), and iE-DAP (Appendix Fig S4C and E). Thus, microbes and NODs agonists induce expression of IRGM that by a negative feedback loop mediates degradation of NODs-RIPK2 signaling proteins to suppress NF- κ B response to maintain cell-autonomous innate immune homeostasis.

IRGM and p62 cooperate to conduct selective autophagy of NODs and RIPK2/RIPosomes

We scrutinized whether IRGM-dependent degradation of NODs and RIPK2 is mediated through proteasome or autophagy. Inhibition of autophagy flux (using Baf A1) but not proteasome (using MG132) restored the IRGM-dependent degradation of NODs and RIPK2 (Appendix Fig S5A-C). Further, the depletion of ATG5 rescued the IRGM-mediated degradation of endogenous (THP-1 cells; Fig EV3A and B) or overexpressed (HEK293T cells) NODs and RIPK2 (Fig EV3C-E). Also, the IRGM-dependent RIPosome degradation is restored when the cells were either depleted of ATG5 or were treated with Baf A1 (Fig EV3F). This and the above-discussed catalytic mutant (IRGM^{S47N}) data demonstrate that IRGM utilizes autophagy to degrade NODs, RIPK2, and RIPosomes. Further, PYR-41 (inhibitor of ubiquitin-activating enzyme E1) rescued the IRGM-mediated degradation of RIPK2, indicating that ubiquitinated RIPK2 is targeted by IRGM-dependent autophagy (Appendix Fig S5D).

Like RIPK2, IRGM interacts only with p62 among the autophagy receptor proteins (Jena *et al.*, 2020). Therefore, we tested whether IRGM cooperates with p62 for the autophagic degradation of RIPK2 and RIPOsomes. First, we investigated whether IRGM, p62, and RIPK2 are present in the same molecular complex. IRGM and p62 were co-localized or juxtaposed to the RIPOsomes (also NOD-RIPOsomes; Fig EV3G and Appendix Fig S5E and F). Also, co-localization/juxtaposition of RIPOsomes, IRGM, and p62 with LC3B was observed (Appendix Fig S5G). Using sequential IP assay, we found that RIPK2, p62, and IRGM were present in the same complex (Fig EV3H). Silencing of p62 rescued the IRGM-dependent autophagic degradation of RIPOsomes (Fig EV3I), and also IRGM-mediated degradation of overexpressed as well as endogenous RIPK2, NOD1, and NOD2 (Fig EV3J–M). Thus, IRGM utilizes p62 adaptor protein to mediate autophagic degradation of NODs, RIPK2, and RIPOsomes. Next, we tested whether IRGM is required for the interaction between p62 and RIPK2. Indeed, the depletion of IRGM reduced the interaction between p62 and RIPK2 (Fig EV3N). Conversely, the presence of IRGM increased the interaction of p62 with NODs and RIPK2 (Fig EV3O–Q).

Taken together, the results show that IRGM and p62 cooperate to conduct inflammophagy of NODs, RIPK2, and RIPOsome complexes. In addition, we observed that autophagy initiation and elongation protein ULK1 and ATG16L1 were co-localized with IRGM over the RIPOsomes (Appendix Fig S5H and I), indicating that IRGM engages canonical autophagy machinery for degradation.

Combined results from this and the previous sections suggest microbes induce RIPOsome formation and IRGM expression. Both IRGMs and RIPOsomes are recruited over bacteria. Where RIPOsome formation induces NF- κ B response, IRGM-dependent autophagic degradation of NODs-RIPK2 complex suppresses the NF- κ B response to balance the inflammatory outputs (Fig EV3R).

IRGM negatively regulates bacteria-induced RIPK2-dependent pro-inflammatory signaling pathways

To understand the role of IRGM in regulating host response to bacterial infection, we performed RNA-sequencing (RNA-seq) experiment with *Salmonella typhimurium* infected control and stable IRGM shRNA knockdown HT-29 colon cells. Hierarchical clustering based on gene ontology (GO) terms was performed using genes differentially regulated ($P < 0.05$, 1.5-fold) in basal and *Salmonella*-infected IRGM-depleted cells compared with controls. Several inflammatory (e.g., Interferon signaling and cytokine signaling) and infection-related processes (e.g. ER-phagosome and antigen processing/presentation) were among the top-enriched pathways (Reactome pathway analysis) induced in IRGM-depleted cells, which were further increased upon *Salmonella* infection (Datasets EV1 and EV2, and Fig EV4A). In basal conditions, IRGM suppresses a large number of IFN-stimulated genes (ISGs; Jena *et al.*, 2020). Here, we found that during *Salmonella* infection, in addition to ISGs, IRGM suppressed a large number of chemokines (*CXCL1*, 2, 3, 5, 6, 8, 10 and *CCL20*, 22, 28, etc.) interleukins (*IL1A*, *IL1B*, *IL1E/36G*, *IL17C*, *IL32*, *IL15*, etc.) and TNF superfamily genes (*TNFSF9*, *TNFSF10*, *TNFSF13*, *TNFSF15*, etc.; Dataset EV3, and Fig EV4B and C). Several other pathways such as endoplasmic reticulum-phagosome response, endosomal/vacuolar pathways, and antigen processing and presentation were upregulated in *Salmonella*-infected IRGM-

depleted cells (Fig EV4A and B). The RNA-seq results were validated by performing qRT-PCR with several chemokines and interleukins (Fig EV4D). Next, to define the IRGM-dependent transcriptome that is exclusively upregulated upon *Salmonella* infection, we filtered out all the basal level differentially upregulated genes and performed Reactome pathway analysis (Fabregat *et al.*, 2018) with the rest of the transcriptome (Dataset EV4). In this analysis, the top-enriched pathways were TNF α signaling, IL-17 signaling, NF- κ B signaling, interleukin-dependent signaling, interferon-gamma response, and NOD-like receptor signaling pathway (Fig EV4E). These data indicate that during bacterial infection IRGM limits an extensive and comprehensive program of pro-inflammatory response including NF- κ B, TNF α , NODs, and IFN signaling pathways.

Our next step was to evaluate the extent to which IRGM-mediated suppression of the inflammatory response was dependent upon NOD1/2-RIPK2 signaling. For that, we performed RNA-seq analysis with *Shigella flexneri* infected WT, IRGM^{+/-}, and RIPK2-depleted IRGM^{+/-} HT-29 cells. To better understand whether the suppression of the pro-inflammatory response by IRGM is specific to *Salmonella* or applies globally, we performed transcriptome analysis on *Shigella*-infected cells. A comparison of the analysis of the transcriptome induced in *Shigella* versus *Salmonella*-infected IRGM-depleted cells suggests that almost similar genes and pathways were upregulated in both the conditions (Fig EV4B vs. F, Dataset EV5), suggesting that IRGM has identical anti-inflammatory functions during different bacterial infections. Next, we performed the analysis with a set of genes that are significantly upregulated in IRGM^{+/-} HT-29 cells (compared with control, $P < 0.05$, 1.5-fold, $n = 3$) and at the same time were significantly rescued by RIPK2 depletion ($P < 0.05$, 0.8, $n = 3$; Dataset EV6). A large number of genes (~250 genes) that were induced upon IRGM depletion were rescued by RIPK2 knockdown, suggesting that IRGM regulates pro-inflammatory responses through modulation of RIPK2 protein levels (Fig 6A and Dataset EV6). Metascape pathway analysis (Tripathi *et al.*, 2015) with this gene set revealed that upon *Shigella* infection, IRGM suppresses several inflammatory responses including IFN response, NF- κ B signaling, and interleukin signaling in a RIPK2-dependent manner (Fig 6B). Several of the NF- κ B-regulated genes such as *NINJ1*, *MAPK11*, and cytokines such as CXCLs (*CXCL1*, 3, 6, 10, and 11), Interleukins (*IL1 α* and *IL1 β*), tumor necrosis factors, and receptors (*TNF- α* , *TNSFAIP's*, and *TNSF's*), that were induced upon IRGM^{+/-} were rescued by additional siRNA knockdown of RIPK2 (Fig 6C and D). Interestingly, during bacterial infection IRGM limited the interferon response in a RIPK2-dependent manner (Fig 6E and F). This was evident by the partial rescue of several sentinels' interferon-responsive genes including *IFITM's*, *GBP's*, *OAS1-3*, *MX1/2*, *ISG15*, and *RSAD2* when RIPK2 is knockeddown in IRGM^{+/-} HT-29 cells (Fig 6E and F). In agreement with these results, TRRUST (database of literature-curated human TF-target interactions; Han *et al.*, 2018) analysis predicted RELA, NF- κ B, and STAT1 as the major transcription factors for this response (Fig EV4G).

Taken together, these results demonstrate that IRGM suppresses multiple inflammatory responses during bacterial infection and limits the array of RIPK2-dependent pro-inflammatory responses.

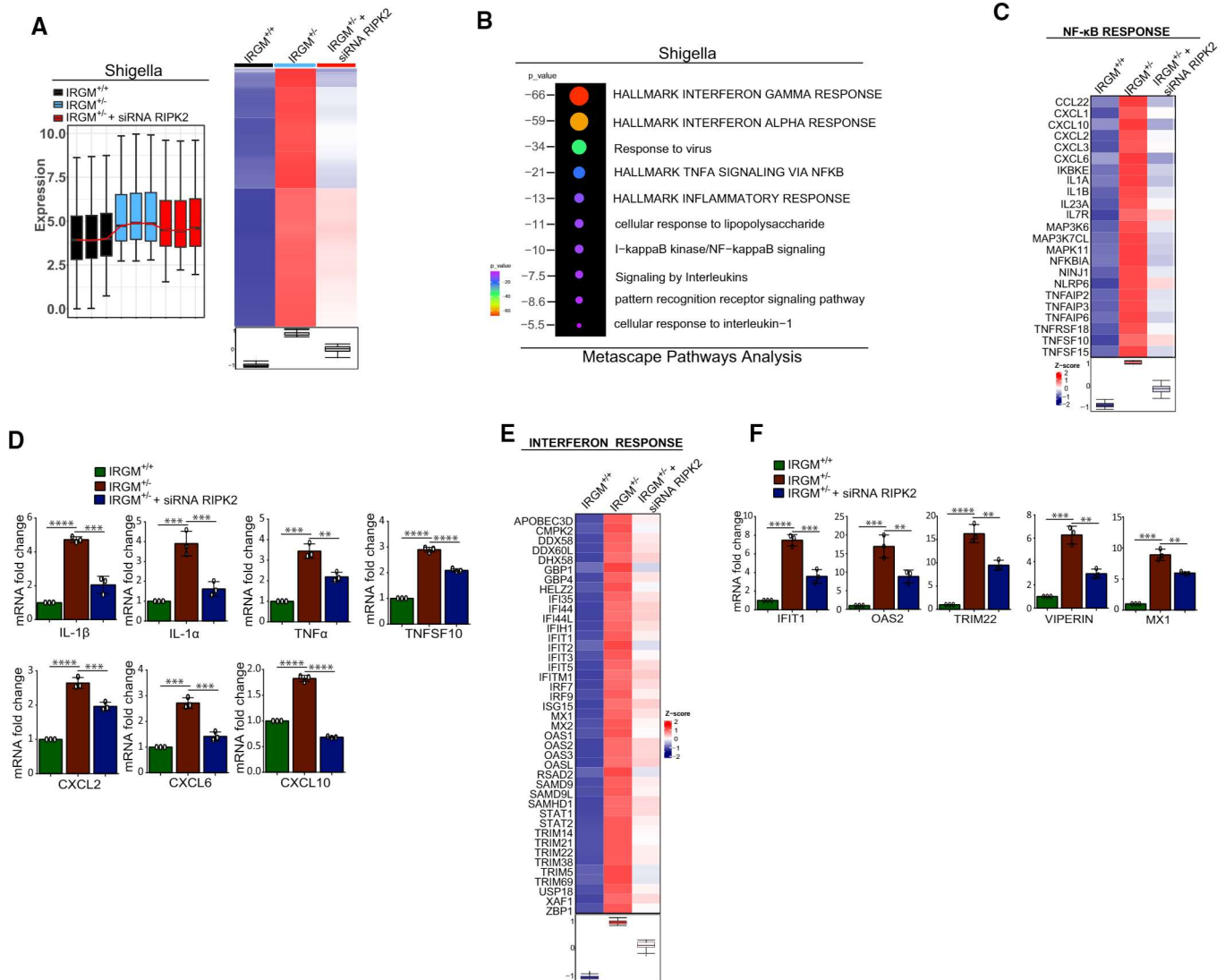


Figure 6. IRGM negatively regulates *Shigella*-induced RIPK2-dependent pro-inflammatory signaling pathways.

A Box plot distribution with normalized log expression (Left panel) and heatmap (Right panel) of the genes that were significantly upregulated in IRGM^{+/-} HT-29 cells (compared with control; 1.5-fold, $P < 0.05$, Wald Chi-Squared test, $n = 3$, biological replicates) and at the same time were significantly rescued by RIPK2 depletion in IRGM^{+/-} HT-29 cells ($P < 0.05$, 0.8 , $n = 3$) infected with *S. flexneri* for 6 h (MOI 1:25). Left panel, the box and whisker plot shows upper and lower quartile of the data-sets. Right panel, the graph below the heat map shows box plot with median obtained from data scaled to Z-score.

B Bubble plot graph depicting the overrepresented pathways (in order of P -value) obtained using Metascape pathway analysis software from the genes significantly upregulated in IRGM^{+/-} cells (compared with control; 1.5-fold, $P < 0.05$, Wald Chi-Squared test, $n = 3$) and at the same time were significantly rescued by RIPK2 depletion in IRGM^{+/-} HT-29 cells ($P < 0.05$, 0.8 , $n = 3$) infected with *S. flexneri* for 6 h (MOI 1:25).

C Heatmap depicting the representative NF- κ B responsive genes that were significantly upregulated in IRGM^{+/-} cells (compared with control; 1.5-fold, $P < 0.05$, Wald Chi-Squared test, $n = 3$ biological replicates) and at the same time were significantly rescued by RIPK2 depletion in IRGM^{+/-} HT-29 cells ($P < 0.05$, Wald Chi-Squared test, 0.8 , $n = 3$ biological replicates). The graph below the heat map shows box plot with median obtained from data scaled to Z-score.

D The qRT-PCR analysis of NF- κ B responsive cytokines and chemokines with total RNA isolated from the *S. flexneri*-infected IRGM^{+/+}, IRGM^{+/-}, and RIPK2-depleted IRGM^{+/-} HT-29 cells. Mean \pm SD, $n = 3$ (biological replicates), $^{**}P < 0.005$, $^{***}P < 0.0005$ and $^{****}P < 0.00005$, ordinary one-way ANOVA (Tukey's multiple comparisons test).

E Heatmap depicting the representative IFN response genes significantly upregulated in IRGM^{+/-} cells (compared with control; 1.5-fold, $P < 0.05$, Wald Chi-Squared test, $n = 3$ biological replicates) and at the same time were significantly rescued by RIPK2 depletion in IRGM^{+/-} HT-29 cells ($P < 0.05$, Wald Chi-Squared test, 0.8 , $n = 3$, biological replicates). The graph below the heat map shows box plot with median obtained from data scaled to Z-score.

F The qRT-PCR analysis of NF- κ B responsive cytokines and chemokines with total RNA isolated from the *S. flexneri*-infected IRGM^{+/+}, IRGM^{+/-}, and RIPK2-depleted IRGM^{+/-} HT-29 cells. Mean \pm SD, $n = 3$ (biological replicates), $^{**}P < 0.005$, $^{***}P < 0.0005$ and $^{****}P < 0.00005$, ordinary one-way ANOVA (Tukey's multiple comparisons test).

Source data are available online for this figure.

RIPK2 inhibition ameliorates shigellosis and DSS-induced gut inflammation in *Irgm1*^{KO} mice

Genetic variations in *IRGM* are associated with increased susceptibility to sepsis, bacterial infections, and gut inflammatory diseases (Massey & Parkes, 2007; Parkes et al, 2007; Intemann et al, 2009; Kimura et al, 2014). Consistently, *Irgm1*^{-/-} mice were found to be more susceptible to DSS-induced colitis (Liu et al, 2013). Since we found that *IRGM* negatively regulates RIPK2-dependent pro-inflammatory responses, we hypothesized that therapeutic inhibition of RIPK2 could reduce gut inflammation associated with *Irgm1* depletion in shigellosis- and DSS-induced colitis models.

For *Shigella* infection in mice, we used the intraperitoneal model of shigellosis (Yang et al, 2014). In both colitis models, *Irgm1*-deficiency significantly accelerated body weight loss (Fig 7A and B) and increased the scores of stool consistency and rectal bleeding (Fig EV5A and B). Treatment of *Irgm1*^{-/-} mice with the RIPK2 inhibitor GSK583 (Haile et al, 2016; Goncharov et al, 2018) significantly ameliorated the acute colitis symptoms (Figs 7A and B, and EV5A and B). Consistently, GSK583 was able to suppress the colon shortening in *Irgm1*^{-/-} mice in both shigellosis- and DSS-induced colitis models (Figs 7C and EV5C). Next, we examined the severity of colon damage and inflammation by histopathological analysis using hematoxylin and eosin (H&E) staining. In *Irgm1*^{-/-} mice, a significant increase in DSS-induced epithelial injury, loss of goblet cells, hyperplasia, and immune cell (neutrophils) infiltration was observed in the colon (Figs 7D and EV5D). Treatment of *Irgm1*^{-/-} mice with GSK583 significantly attenuated histopathology and immune cell invasion (Figs 7D and EV5D). Similarly, *Shigella*-induced colon histopathology in *Irgm1*^{-/-} mice was significantly improved by treatment with GSK583 (Fig EV5E and F).

An enhanced oligomerization of RIPK2 was observed in *Irgm1*^{-/-} mice colon lysates that were dampened by the administration of GSK583 in these mice (Fig 7E). The increased levels of NF-κB (IL1α, IL1β, and TNF-α) and IFN (MX1, IFIT1, and ISG15) dependent cytokine response in *Irgm1*^{-/-} mice colon were suppressed by treatment of GSK583 in both shigellosis- and DSS-induced colitis models (Figs 7F and EV5G). Immunohistochemistry analysis showed enhanced staining of IL1β in *Irgm1*^{-/-} mice colon that was significantly reduced in GSK583-treated *Irgm1*^{-/-} mice (Fig 7G). The enhanced expression of ISG15, RSAD2 (Viperin), and protein ISGylation (IFN response markers) in *Irgm1*^{-/-} mice colon was

considerably reduced upon treatment with GSK583 (Fig 7H). Similarly, GSK583 administration considerably diminished the increased protein levels of pro-caspase-1, cleaved caspase-1, phospho-p65, and phospho-p38MAPK in *Irgm1*^{-/-} mice colon (Fig 7H and I).

Taken together, the data show that RIPK2 inhibition can ameliorate the gut inflammation and pathology associated with *Irgm1* deprivation in mouse colitis models.

Discussion

In this study, we made two major advances in understanding the regulation of NODs-RIPK2-NF-κB signaling. First, we revealed that when pathogenic bacteria infect cells, RIPK2 forms RIPosomes, which recruit over the bacteria and induce NF-κB response. Second, we show that autophagy suppresses NF-κB pro-inflammatory signaling by selectively degrading NODs, RIPK2, and RIPosomes. Consequently, this study demonstrates how the two cells' autonomous systems that are loaded over the bacteria work in concert for innate immune defense against the pathogens and cutting down excess inflammation as a safeguard.

The cryogenic electron microscopic (Cryo-EM) structure of RIPosomes was illustrated by two recent studies (Gong et al, 2018; Pellegrini et al, 2018). They found that RIPK2 forms a filamentous structure in cells using its CARD domain. Interestingly, the helical symmetry of RIPosomes and ASC filaments (Lu et al, 2014) was found to be strikingly similar suggesting that their assembly is governed by a similar mechanism. Further, they suggest that the CARDS of NOD1/2 may transiently interact with the CARD of RIPK2 to induce their oligomerization, similar to the phenomenon observed in RIG-I-MAVS signaling complexes (Wu & Hur, 2015). We found that RIPK2 can self-polymerize; however, both NOD1 and NOD2 failed to do so unless co-expressed with RIPK2. This is consistent with previous studies that suggest that NOD1/2 has a low propensity to self-associate (Fridh & Rittinger, 2012; Gong et al, 2018). Taken together, it appears that NODs monomers trigger RIPK2 oligomerization, which in turn increases the propensity of NODs to oligomerize and form NODo-RIPosomes.

Ellwanger et al, 2019 demonstrated that XIAP controls RIPK2 signaling by preventing its depositions in speck-like structures. Given the role of XIAP in autophagy, it will be interesting to determine whether XIAP has a role in the autophagic degradation of RIPosomes.

Figure 7. RIPK2 inhibition ameliorates shigellosis- and DSS-induced gut inflammation in *Irgm1* knockout mice.

- A, B Upper panels, schematic representation of shigellosis- and DSS-induced colitis models used. In lower panels, the graph depicts percentage loss in body weight in *Irgm1*^{+/+} and GSK583 untreated or treated *Irgm1*^{-/-} mice when (A) infected with *S. flexneri* ($n = 6$ mice) or (B) administrated with DSS ($n = 3$ mice). Mean \pm SD, * $P < 0.05$, ** $P < 0.005$, Student's unpaired t -test.
- C Left panel, representative pictures of colons of *Irgm1*^{+/+} and *Irgm1*^{-/-} mice untreated or treated with GSK583 infected with *S. flexneri*. Right panel, the graph depicts the average colon lengths of the mice groups. Mean \pm SD, $n = 6$, ** $P < 0.005$, *** $P < 0.0005$, Student's unpaired t -test.
- D Representative microscopic images of H&E staining of colon tissues of *Irgm1*^{+/+} and *Irgm1*^{-/-} mice untreated or treated with GSK583 administrated with DSS. The graph depicts the combined histological scores. Mean \pm SD, $n = 3$ (DSS), ** $P < 0.005$, Student's unpaired t -test. Scale bar, 200 μ m.
- E The soluble and insoluble fractionations of lysates from colon tissues of *Shigella*-infected or DSS-treated *Irgm1*^{+/+} and *Irgm1*^{-/-} mice treated with GSK583 as indicated, were subjected to immunoblot analysis with indicated antibodies.
- F The qRT-PCR analysis with total RNA isolated from the colon tissues of *S. flexneri*-infected *Irgm1*^{+/+} or *Irgm1*^{-/-} or GSK583-treated *Irgm1*^{-/-} mice. Mean \pm SD, $n = 6-8$, * $P < 0.05$, ** $P < 0.005$, *** $P < 0.0005$, ordinary one-way ANOVA (Tukey's multiple comparisons test).
- G Representative confocal images of IL-1β immunostained colon tissues of DSS-treated *Irgm1*^{+/+} or *Irgm1*^{-/-} or GSK583-treated *Irgm1*^{-/-} mice. Scale bar, 10 μ m.
- H, I Western blot analysis with the colon tissue lysates of DSS-treated or *S. flexneri*-infected mice groups as indicated.

Source data are available online for this figure.

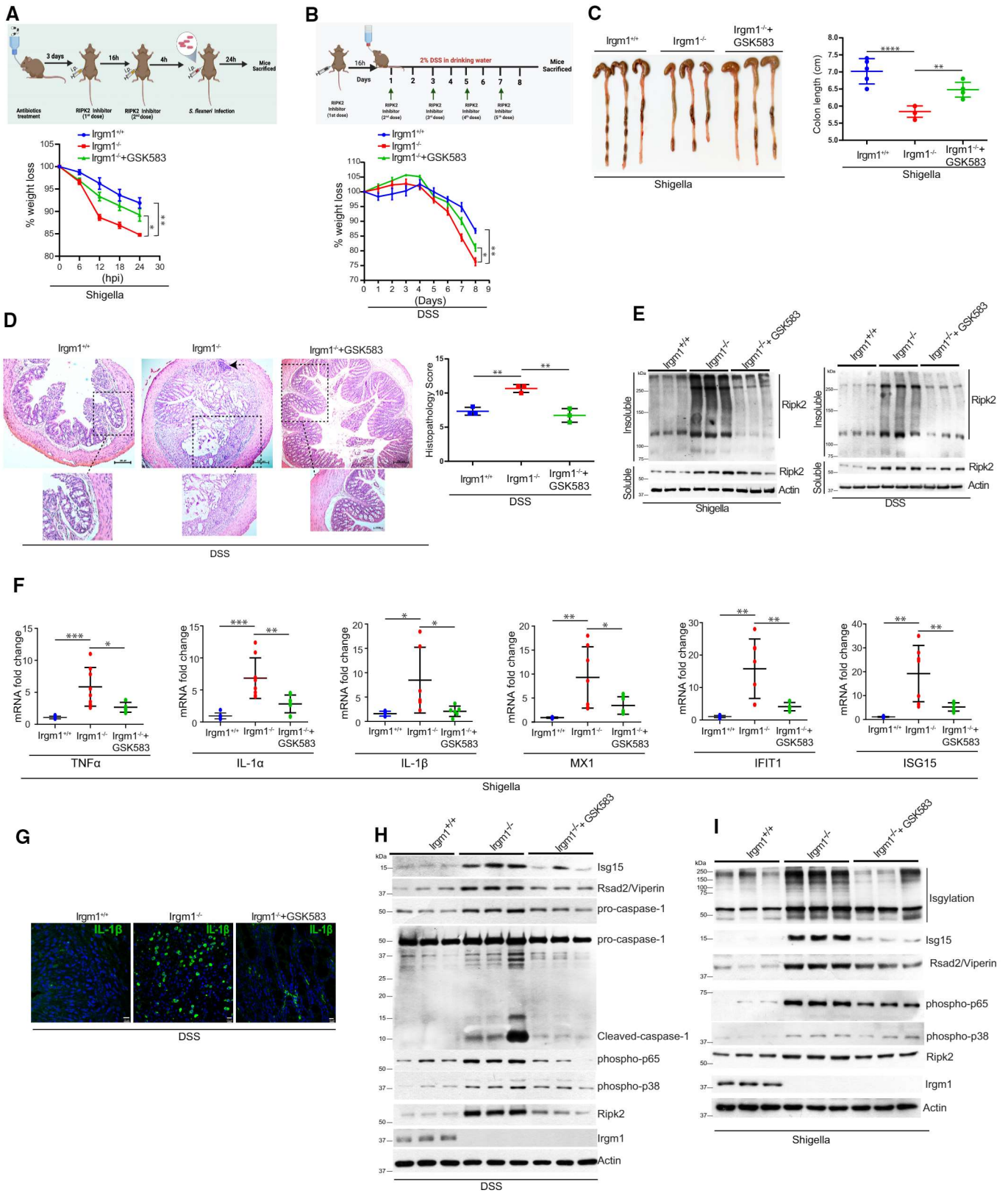


Figure 7.

We found that upon bacterial infection endogenous RIPK2 undergoes oligomerization to form RIPosomes in macrophages. Also, we found that pathogenic bacteria have a greater ability to induce RIPosome formation than nonpathogenic bacteria. At present, we do not understand the basis of this difference as both pathogenic and nonpathogenic bacteria produce ligands for NODs activation. It could be a possibility that, in addition to these ligands, some other bacterial factors are required to induce endogenous oligomerization of RIPK2. Consistently, the NODs agonist, MDP, or iE-DAP were inefficient in inducing RIPosome formation. Further studies are needed to identify the bacterial factors that enhance RIPosomes biogenesis. RIPosomes were either juxtaposed or recruited over the pathogenic bacteria. While NODs puncta co-localize with RIPosomes over bacteria, they are less consistent than RIPosome depositions suggesting that like RIG-I-MAVS interaction (Wu & Hur, 2015), NODs might transiently interact with RIPK2 to activate it.

The NODs-RIPK2-dependent NF- κ B pro-inflammatory response is important to eliminate the invading pathogens. However, extensive inflammation could be deleterious and lead to immuno-pathologies. To prevent damage, cells employ several cell-autonomous mechanisms to tone down the inflammation. Genetic mutations in components of the NODs-RIPK2-NF- κ B pathway predispose toward chronic autoimmune and inflammatory diseases (Miceli-Richard et al, 2001; Kanazawa et al, 2005; Henckaerts & Vermeire, 2007; Caso et al, 2015; Taniguchi & Karin, 2018). Therefore, it is critically important to understand the mechanisms that negatively control this pathway. Autophagy plays a significant role in suppressing inflammation and maintaining innate immune balance in the cell by degrading multiple inflammatory proteins/complexes (Chauhan et al, 2021; Deretic, 2021). Our previous study showed that IRGM act as a scaffold protein to bring NOD2-dependent bacterial sensing and autophagy machinery together to conduct antimicrobial defense (Chauhan et al, 2015). Here, we found that IRGM utilizes autophagy machinery to dampen the NOD2-RIPK2-dependent inflammation induced by pathogenic bacteria. Together, it emerges that IRGM has a dual function during bacterial infection. On the one hand, it leads to the clearance of intracellular bacteria by inducing xenophagy, and on the other hand, it reduces inflammation by inducing autophagic degradation of NODs and RIPK2.

IRGM is a genetic risk factor for several inflammatory and infectious diseases including inflammatory bowel disease, and tuberculosis (Massey & Parkes, 2007; Parkes et al, 2007; Lu et al, 2013; Kimura et al, 2014; Lin et al, 2016; Xia et al, 2017; Yao et al, 2018). The depletion of *Irgm1* in mice triggers inflammasome and IFN responses leading to autoimmune-like conditions. Depletion of IRGM led to upregulation of several inflammatory responses including NF- κ B and IFN responses in a RIPK2-dependent manner that is blocked by chemical inhibition of RIPK2. These data suggest that RIPK2 inhibitors could be used as therapeutic options in patients with inflammatory diseases caused by the loss of function of IRGM.

Materials and Methods

Cell culture

All the common cell lines including THP-1 (ATCC TIB-202), HT-29 (ATCC HTB-38), and HEK293T (ATCC CRL-3216) cells

were obtained from the American Type Cell Culture (ATCC), US. HEK-Blue hNOD2 cells were purchased from InvivoGen and maintained as per the instructions. HT-29, HEK293T, and HeLa cells were maintained in DMEM (GIBCO) supplemented with 10% heat-inactivated fetal bovine serum (FBS) and penicillin/streptomycin. THP-1 cells were maintained in RPMI-1640 (GIBCO) supplemented with 10% heat-inactivated FBS, Glucose (5%), HEPES buffer (10 mM), L-glutamine (5 mM), sodium pyruvate (1 mM), and penicillin/streptomycin. All the cell lines were tested for mycoplasma contamination routinely (every 2–3 months). All the experiments were performed with cells below the 20th passage.

Generation of CRISPR/Cas9 KO cell lines

The RIPK2 knockout HT-29 cell line is generated using the CRISPR-Cas9 method. Briefly, HT-29 cells seeded in 6-well plates and transfected with RIPK2/RICK Double Nickase Plasmid (Santacruz; sc-400,731-NIC) using ViaFect transfection reagent (Promega # E4981). After 48 h, GFP-positive cells were sorted into 96-well plates using MoFlo Asterio cell sorter (Beckman Coulter Life Sciences). The cells were grown in a growth medium containing 1 μ g/ml puromycin for 1 week. The individual clones were selected and screened for knockout using Western blot analysis. The IRGM knockout HT-29 cell line was generated as described previously (Jena et al, 2020).

Inhibitors and reagents

N-Acetylmuramyl-L-alanyl-D-isoglutamine, MDP (InvivoGen # tlr-mdp); γ -D-glutamyl-meso-diaminopimelic acid, iE-DAP (InvivoGen # tlr-dap); 6-[(1,1-dimethylethyl) sulfonyl]-N-(5-fluoro-1H-indazol-3-yl)-4-quinolinamine, GSK583 (Cayman # 19739); Phorbol 12-myristate 13-acetate, PMA (Sigma # P8139); Bafilomycin A1 (CST# 54645S); Z-leu-leu-leu-al, MG132 (Sigma # C2211-5MG); Dextran sulfate sodium salt, DSS (MP Biomedicals # 160110), Ubiquitin E1 Inhibitor, PYR-41 (Sigma # 662105), ProLong Gold antifade reagent with DAPI (Invitrogen # P36931), ProLong Gold antifade reagent (Invitrogen # P36930).

Soluble-insoluble fractionation

For soluble-insoluble protein fractionation, cells were lysed in 1% Triton X-100 lysis buffer containing 150 mM NaCl, 50 mM Tris (pH 7.5), 10% glycerol, 1 mM EDTA, 1 mM PMSF, and protease inhibitor cocktail at 4°C for 20 min followed by centrifugation for 10 min at 17,000 g at 4°C. After centrifugation, the supernatant was used as a soluble fraction and the pellet was resuspended in lysis buffer with 1% SDS and used as an insoluble fraction for Western blot analysis.

Nuclear and cytoplasmic fractionation

Nuclear and cytoplasmic fractionation assay was performed using the NE-PER Nuclear and Cytoplasmic Extraction Reagents (Thermo-Fisher Scientific # 78833) according to the manufacturer's protocol. Briefly, 2×10^6 HeLa cells were infected with *S. flexneri* (MOI 1:25) for 4 h. The cells were harvested with trypsin-EDTA and centrifuged at $500 \times g$ for 5 min. The cell pellet was washed with $1 \times$ PBS and resuspended in 200 μ l CER I, vortexed vigorously for 15 s, and incubated on ice for 10 min. After the incubation, 11 μ l of ice-

cold CER II were added to each sample, vortexed followed by incubation on ice for 1 min. The samples were centrifuged at $16,000 \times g$ for 5 min to extract cytoplasmic fraction (supernatant) and the pellet (insoluble fraction) was resuspended in 100 μ l NER, vortexed, incubated on ice with intermittent vortexing for 40 min. The samples were centrifuged at $16,000 \times g$ for 10 min at 4°C to isolate nuclear fraction and subjected to western blot analysis.

Cycloheximide chase assay

Approximately, 2×10^6 HT-29 cells were plated in a 6-well plate and grown overnight. The next day, cells were treated with cycloheximide (100 μ g/ml) with or without Bafilomycin A1 (300 nM) or MG132 (20 μ M) for various time points. The cells were lysed in NP-40 lysis buffer containing 1 \times protease inhibitors cocktail and 1 mM PMSF and subjected to Western blotting with indicated antibodies.

Western blotting

The cells were lysed using NP-40 lysis buffer (Invitrogen # FNN0021) containing 1 mM PMSF (Sigma # P7626), phosSTOP (Roche # 49068455001), and protease inhibitors cocktail (Roche # 1183617000). Mice tissue were homogenized in radio-immunoprecipitation assay (RIPA) buffer (20 mM Tris, pH 8.0; 0.5 EGTA; 1 mM EDTA; 150 mM NaCl; 1% IGEPAL (Sigma); 10% glycerol; 0.1% Sodium deoxycholate). The protein concentration in the lysate was determined using the BCA method (Pierce™ BCA Protein Assay Kit # 23225). Lysates were separated using SDS-PAGE, transferred onto a nitrocellulose membrane (Bio-Rad), and blocked for 1 h in 5% skimmed milk followed by incubation in primary antibody overnight at 4°C. The membrane was washed with 1 \times PBS/PBST three times and then incubated with HRP conjugated secondary antibody for 1 h at room temperature. After washing with 1 \times PBS/PBST, the blots were developed using enhanced chemiluminescence reagents.

Immunofluorescence assay

Approximately, HEK293T/HeLa 10^5 cells were seeded on a coverslip and allowed to adhere overnight before transfection with plasmids. For THP-1 cells, approximately, 5×10^5 cells were treated with 50 ng/ml of PMA (Sigma # P8139) and seeded on the coverslip for differentiation into macrophages for 16 h. After a resting period of 24 h, cells were treated with stimulants or infected as required. The cells were fixed in 4% paraformaldehyde for 15 min, permeabilized with 0.1% Triton X-100 (or 0.1% saponin) for 15 min, followed by blocking with 1% bovine serum albumin (BSA) for 30 min at room temperature (RT). The permeabilized cells were then incubated with primary antibody as indicated for 1 h at RT or overnight at 4°C, washed thrice with 1 \times PBS, followed by incubation with Alexa fluor-conjugated secondary antibodies for 1 h at RT. The cells were washed thrice with 1 \times PBS, mounted with ProLong™ Gold antifade mountant with or without DAPI, air-dried, and visualized using a super-resolution Leica SP8 lightning confocal microscope.

Proximity ligation assay (PLA)

Proximity ligation assay (PLA) was performed using a Duolink *in situ* detection kit as per the manufacturer's protocol (Sigma

#DUO92008). Briefly, 2×10^5 HEK293T cells were seeded on the coverslip and allowed to adhere overnight before transfection with the desired plasmids. After 12 h of transfection, cells were fixed with a 4% paraformaldehyde solution. Next, antigen retrieval was performed in sodium citrate buffer (10 mM, pH 6.0) and the cells were permeabilized with 0.1% Triton X-100 followed by blocking with 1 \times blocking solution (provided with the kit) in a preheated humidity chamber for 1 h at 37°C. The cells were incubated overnight with primary antibody diluted with diluent at 4°C. Next, the coverslips were washed twice with 1 \times wash buffer-A followed by incubation with Duolink *in situ* PLA probes in a preheated humidity chamber for 1 h at 37°C. After PLA probe incubation, coverslips were washed twice with 1 \times wash buffer-A followed by ligation with Duolink *in situ* ligase for 30 min in a preheated humidity chamber at 37°C. Next, coverslips were washed twice with 1 \times wash buffer-A followed by amplification through Duolink *in situ* polymerase for 90 min in a preheated humidity chamber at 37°C. Final washing was done twice with 1 \times and 0.01 \times wash buffer-B. The coverslips were mounted over glass slides using Duolink *in situ* mounting media with DAPI and the edges of the coverslip were sealed, mounted, and visualized using a Leica SP8 confocal microscope.

High-content microscopy imaging

For high-content microscopy imaging, approximately 17,000 HEK293T cells, 8,000 HeLa cells, and 50,000 PMA-treated THP-1 cells were seeded in a black flat bottom 96-well plate (Thermo Scientific, Nunc) and transfected with plasmids or treated or infected as indicated. The cells were fixed with 4% PFA and permeabilized with 0.1% Triton X-100 for 15 min, followed by blocking with 1% bovine serum albumin (BSA) for 30 min and incubation with primary antibody for 1 h. The cells were washed thrice with 1 \times PBS and incubated with secondary antibody for 1 h and then counterstained with 0.5 μ g/ml of DAPI for 5 min. Imaging was performed by using Cell insight CX7 LZR high-content screening platform (Thermo Scientific). Automated image scanning and analysis were carried out using HCS studio and iDEV software, respectively. Automated images were captured at 10 \times (or 20 \times) by taking 1,500–20,000 cells and 35 fields per well or as indicated in figure legends. Images were quantified using scanning parameters and object mask definitions. A threshold value was set to find out the primary objects (cells). DAPI staining was used for autofocus and identification of the primary objects. The cells and regions of interest (ROI) or desired targets were further validated by total area, shape/segmentation, maximum/minimum average intensity, and total intensity. By using the cell mask and intensity of the puncta, the number of puncta per cell was counted. All data processed and analyzed were computer-based.

Hematoxylin and eosin (H&E) staining and immunohistochemistry analysis for mice colon tissue

The colon sections were deparaffinized and hydrated through an alcohol gradient followed by 1 \times PBS wash. For hematoxylin and eosin staining, the sections were stained with hematoxylin for 5 min followed by washing in water to remove excess stain. The sections were then incubated in Scott's tap water followed by staining with Eosin dye. The slides were washed, dehydrated in absolute ethanol, cleared in xylene, and mounted with DPX. Finally, slides were observed under Zeiss Apotome 2.0 microscope.

For immunohistochemistry, colon sections were deparaffinized and hydrated through ethanol gradient followed by 1× PBS wash. Antigen retrieval was performed in sodium citrate buffer (pH 6.0) for 10 min followed by permeabilization with 1× PBS (pH 7.4) containing 0.25% Triton X-100, blocked with goat serum. The slides were washed for 2 min thrice with PBS (pH 7.4) containing 0.05% Tween 20 followed by incubation of sections with an unconjugated affinity purified F(ab) fragment anti-mouse IgG (H + L) (Abcam #ab6668) for 1 h at room temperature. The sections were incubated overnight at 4°C with antibodies as indicated. The next day, the sections were washed twice with 1× PBS (pH 7.4) containing 0.05% Tween 20, followed by incubation with goat anti-rabbit/mouse IgG (H + L) Alexa Fluor 488/568 conjugated secondary antibody for 1 h. Sections were again washed and counterstained with DAPI for 1 min followed by incubation with an auto-fluorescence quencher (Vector Labs #SP-8400). Sections were finally mounted with Vectashield Vibrance Antifade mounting media. The slides were visualized under Leica TCS SP8 STED confocal microscope.

Co-immunoprecipitation assay

The cells were lysed in NP-40 lysis buffer containing 1× protease inhibitors cocktail and 1 mM PMSF for 20 min at 4°C and centrifuged at 12,000 g for 30 min at 4°C. The supernatant was incubated with the antibody at 4°C for 2 h on a rotational cell mixer followed by incubation with protein G Dynabeads (ThermoFisher#10003D) for 2 h at 4°C on a rotational cell mixer. The beads were washed with ice-cold 1× PBS four times, and the proteins were eluted from the beads in 2× SDS–PAGE Laemmli buffer by boiling for 5 min for Western blot analysis.

Glutathione S-Transferase (GST)-pull-down assay

The glutathione S-transferase (GST) pull-down assay was performed according to the previously described methods (Mehto *et al.*, 2019a, 2019b). Briefly, GST or GST-RIPK2 or GST-IRGM recombinant proteins were expressed in *E. coli* SoluBL21 (Amsbio), and the proteins were purified on Glutathione Sepharose 4 Fast-Flow beads (GE Healthcare). The [³⁵S] labeled- Myc-NOD1, Myc-NOD2, Myc-RIPK2, Myc-ULK1, Myc-ATG16L1 or Myc-Becclin-1 proteins were *in vitro* translated using TnT T7-coupled reticulocyte lysate system (Promega). The GST proteins were incubated with [³⁵S]-labeled proteins in 200 μl of NETN-E buffer (50 mmol/l Tris, pH 8.0, 100 mm NaCl, 6 mm EDTA, 0.5% NP-40, and 1 mm dithiothreitol (DTT) supplemented with complete mini EDTA-free protease inhibitor cocktail; Roche) for 2 h at 4°C. After incubation, the beads were washed five times with NETN-E buffer, boiled with loading buffer, and subjected to SDS–PAGE. The gels were stained with coomassie blue and vacuum-dried. The GST was detected by staining with coomassie blue stain, whereas the [³⁵S]- labeled Myc-tagged proteins were detected in PharosFX imager (Bio-Rad Laboratories).

Antibodies and dilutions

Western blotting:

IRGM (Abcam # 69494; 1:500), NOD1 (CST# 3545S; 1:1000), NOD2 (Proteintech # 20980-1-AP; 1:1000), RIPK2 (CST#4142S; 1:1000), Anti-beta Actin (Abcam # ab6276; 1:5000), GFP (Abcam # ab290; 1:5000),

Flag M2 (Sigma # F3165; 1:1000), p62 (BD Biosciences # BD-610832; 1:1000), ATG5 (CST # 2630S; 1:1000), c-Myc (Santa Cruz # sc-40; 1:1000), HA-Tag (CST # 3724S; 1:1000), RICK (Santa Cruz # sc-22,763; 1:1000), Anti-LC-3B antibody (Sigma # L7543; 1:1000), Anti-RICK A-10 (Santa Cruz # sc-166,765; 1:1000), IL-1β (CST#12242), Anti-pro Caspase1 + p10 + p12 Antibody (Abcam # ab179515; 1:1000), ISG15 (Santa Cruz# sc-166755; 1:500), Phospho-p38 MAPK (Thr180/Tyr182; 1:1000; CST#9211; 1:1000), Phospho-NF-κB p65 (ser536) (93H1) (CST# 3033; 1:1000). HRP conjugate secondary antibodies were purchased from Novus (1:2000) or Promega (1:5000).

Immunofluorescence

IRGM (Santa Cruz #68202; 1:50), RICK H-300 (Santa Cruz # sc-22,763; 1:100), NOD2 (Millipore # 04-145; 1:50), p62 (BD Biosciences # BD-610832; 1:250), LC3b (Sigma # L7543; 1:250), LC3b (MBL # PM036; 1:100), LAMP2A (Abcam # ab18528; 1:50), EEA1 (CST # 3288; 1:50), FK2 (MBL # D058-3;1:250), LC3b (CST # 83506, 1:50), IL-1β (CST # 12242), ULK1 (Santa Cruz # 33182; 1:100), c-Myc (Santa Cruz # sc-40; 1:500), Flag M2 (Sigma # F3165; 1:250), Alexa fluor Secondary antibodies (1:2000) were purchased from Thermo Fisher Scientific.

Plasmids and deletion constructs

The mcherry-RIPK2, GFP-RIPK2 and its deletion construct, GFP-NOD1 and its deletion construct and GFP-NOD2 were generated using gateway cloning strategy as per standard protocols (Invitrogen). pGL4.32[luc2P NF-κB-RE Hygro] purchased from Promega (Promega # E8491).

Transient transfection with siRNA

The THP-1 cells were electroporated using the Neon transfection system (Invitrogen # MPK5000; setting: 1400 V, 10 ms, 3 pulses, 100 μl tip) with 30 nM siRNA or as indicated: nontargeting siRNA, p62 siRNA (SASI_Hs01_00118616), IRGM siRNA (SASI_HS02_00518571), ATG5 (SASI_Hs01_00173156), human RIPK2 siRNA (SASI_Hs01_00199696), mice RIPK2 siRNA (SASI_Mm01_00188069) from Sigma-Aldrich. After 24-h transfection, one more time transfection was performed in a similar condition and incubated for an additional 48 h before the start of each experiment. The HT-29, HeLa, and HEK293T cells were transfected with 30 nM siRNA using Lipofectamine RNAiMAX transfection reagents (Invitrogen# 13778075) as per the manufacturer's instructions.

Transient transfection with plasmid

For transient transfection in THP-1, cells were electroporated using the Neon transfection system (Invitrogen # MPK5000; setting: 1400 V, 10 ms, 3 pulses, 100 μl tip). For overexpression experiments in HEK293T cells, required plasmids were transfected using the calcium phosphate method as per the manufacturer's instruction (Clontech, Promega).

Flag-RIPK2 protein electroporation

Approximately, 2×10^6 HEK293T cells transiently expressing pGL4.32NFκB-RE reporter plasmid electroporated with 10 μg

Purified Flag-RIPK2 in 100 μ l neon resuspension buffer (setting: 1300 V, 10 ms, 1 pulse, 100 μ l tip). The cells were harvested 6-h postelectroporation, and a luciferase assay was performed as described below.

NF- κ B reporter assay

The NF- κ B reporter assay was performed using a luciferase assay kit (Promega) according to the manufacturer's instructions and as described previously (Jena *et al*, 2020). Briefly, HEK293T cells were seeded into the 24-well plate. The next day, cells were transfected with pGL4.32 NF- κ B-RE (Addgene100 ng) together with required plasmids using the calcium phosphate method. After 9 h, the growth medium was removed and cells were washed thrice with 1 \times PBS and lysed using 100 μ l (1X) passive lysis buffer (Promega). The cell lysates were cleared by centrifugation at 12,000 g for 30 s at 4°C, and protein concentration was estimated using the BCA method. In a 96-well plate, 15 μ g/20 μ l lysate mixed with 100 μ l LARII reagent and luminescence measurement was performed using a PerkinElmer VICTOR Nivo Multimode plate reader.

Secreted embryonic alkaline phosphatase (SEAP) reporter assay

Approximately, 3×10^5 HEK293-hNOD2 Blue cells were plated in a 6-well culture plate and incubated at 37°C in a 5% CO₂ incubator overnight. The next day, cells were transfected with the plasmids as indicated using the calcium phosphate method as per the manufacturer's instruction (Clontech, Promega). Six-hours post-transfection, the cell culture medium was replaced with fresh medium with or without L-18 MDP (100 ng/ml) and incubated at 37°C in a 5% CO₂ incubator for 24 h. SEAP activity was determined using QUANTI-Blue reagent as per the manufacturer's instruction. Briefly, in a flat bottom 96-well plate, 20 μ l of sample supernatant was mixed with 180 μ l of QUANTI-Blue solution and incubated for 30 min at 37°C. Optical density (OD) was measured at 620–655 nm using a microplate reader (Bio-Rad).

RNA isolation and quantitative real-time PCR

The total RNA was extracted using TRIzol™ isolation reagent (Invitrogen # 15596026) according to the manufacturer's protocol. One to two microgram of total RNA was used to synthesize cDNA using the high-capacity cDNA synthesis kit (Applied Biosystem #4368813), and qRT-PCR was performed using Power SYBR green PCR master mix (Applied Biosystem #4367659) or TaqMan master mix (Applied Biosystem # 4369016) according to the manufacturer's protocol. The assay was normalized using the housekeeping gene (GAPDH or β -Actin). The fold change in gene expression was calculated by the $2^{-\Delta\Delta C_t}$ method. The graphs were generated using Graph Pad software. The sequence for human and mouse qRT-PCR primers is shown in Appendix Table S1.

RNA-sequencing sample preparation

The total RNA was extracted from the cells using an RNeasy mini kit (QIAGEN #74104). The quality and quantity of RNA were checked using agarose gel and Qubit 3.0. After assessing the quality of RNA, ~850 ng of total RNA was taken for library preparation

using NEBNext®Ultra™ II Directional RNA Library kit for Illumina® (# E7760L) and NEBNext® Poly (A) mRNA Magnetic Isolation Module (# E7490L) as per manufacturer's protocol. The prepared library was quantified using a Qubit dsDNA assay kit (Invitrogen, Q32851) followed by a quality check (QC) and fragment size distribution using a High Sensitivity Tape station Kit (Agilent 2200, 5067–5585, and 5067–5584). The library was sequenced using the HiSeq 4000 Illumina platform.

RNA-sequencing data processing and gene expression analysis

The paired-end (PE) reads quality checks for each sample were performed using FastQC v.0.11.5 (<http://www.bioinformatics.babraham.ac.uk/projects/fastqc/>). The adapter sequence was trimmed using the BBDuk version 37.58, and the alignment was performed using STAR v.2.5.3a with default parameters (Dobin *et al*, 2013) with human hg38 genome build, gencode v21 gtf 9GRCh38 from the gencode. Duplicates were removed using Picard-2.9.4 (<https://broadinstitute.github.io/picard/>) from the aligned files, and read counts were generated using featureCount v.1.5.3 from subread-1.5.3 package (<https://bioweb.pasteur.fr/packages/pack@subread@1.5.3>) with Q = 10 for mapping quality. The count files were used as input for downstream differential gene expression analysis with DESeq2 version 1.14.1 9. (Love *et al*, 2014). The genes with read counts of ≤ 10 in any comparison were removed followed by count transformation and statistical analysis using DESeq “R.” The “P” values were adjusted using the Benjamini and Hochberg multiple testing correction (Haynes, 2013), and the differentially expressed genes were identified (fold change of ≥ 1.5 , P -value < 0.05). A unified nonredundant gene list was made for differential comparisons and subjected to gene ontology (GO) analysis using reactome database (<https://reactome.org/>). The top pathways ($P < 0.05$) were used for generating heat maps using ComplexHeatmap (Version 2.0.0) through unsupervised hierarchical clustering. The expression clusters were annotated based on enriched GO terms. Normalized gene expression was used to generate the boxplots with median depicting the trends in the expression across the different conditions using ggplot2 [version 3.3.5]. The pathways analysis was performed using Metascape database (<https://metascape.org/gp/index.html#/main/step1>). The top pathways ($P < 0.05$) were taken for constructing bubble plots using ggplot2 [version 3.3.5].

The basal conditions groups (for the *Salmonella* infection group) for the dataset E-MTAB-12074 are the same as described previously (Jena *et al*, 2020) and deposited under the accession number E-MTAB-9142 (<http://www.ebi.ac.uk/arrayexpress/experiments/E-MTAB-9142>). The RNA-sequencing experiment for the basal conditions (dataset E-MTAB-9142) and *Salmonella*-infected conditions (dataset E-MTAB-12074) was performed together. However, we have used basal conditions groups' dataset E-MTAB-9142 in our previous publication (Jena *et al*, 2020) and reanalyzed it here along with *Salmonella*-infected dataset E-MTAB-12074.

Bacterial strains and infection of cells in culture

Escherichia coli DH5 α , *Salmonella typhimurium* strain ST 1433, and *Shigella flexneri* (MTCC:1457) (gifted by Dr. Suraj Kumar Tripathy, KIIT, India) were cultured in Luria-Bertani (LB) overnight at 37°C with shaking. Bacteria were subcultured (1:100 dilution) in fresh LB

broth and grown until OD₆₀₀ reached 0.4–0.6. *Mycobacterium smegmatis* MC² 155 and *Mycobacterium tuberculosis* H37Rv (gifted by Dr. Sunil Raghav, ILS, India) were grown in Middlebrook 7H9 liquid medium supplemented with 5 g/l albumin, 2 g/l dextrose, and 0.003 g/l catalase along with 0.05% tween 80.

For fluorescence microscopy, THP-1 cells were treated with PMA (50 ng/ml) and seeded onto glass coverslips in 12-well plates and kept for differentiation. After 16 h, the medium was replaced with fresh medium and incubated for another 24 h. Cells were infected with *Shigella flexneri* 1457 (MOI, 1:25 or 1:50), *Salmonella typhimurium* strain ST 1433 (MOI, 1:10), *E. coli* LF-82 (MOI, 1:10), *Mycobacterium smegmatis* MC² 155 (MOI, 1:10), and *Mycobacterium tuberculosis* H37Rv (MOI, 1:10). Infection was facilitated by centrifugation at 700 × g for 10 min at room temperature and proceeded for 2 h at 37°C on 5% CO₂ incubator. Infected cells were washed three times with 1× PBS and fixed with 4% paraformaldehyde for 30 min at room temperature.

For the RNA-sequencing experiment, approximately 3 × 10⁶ HT-29 cells were seeded in a 60 mm dish and allowed to adhere overnight. The cells were infected with *Shigella flexneri* 1457 (1:25 MOI, 6 h) or *Salmonella typhimurium* strain ST 1433 (MOI, 1:10, 8 h).

Intraperitoneal *Shigella* infection in mice

The mice experiments were performed with the procedure approved by the institutional animal ethical committee at the Institute of Life Sciences (ILS), Bhubaneswar, India. The mice were housed at the animal house facility of ILS. C57BL/6 wild-type and *Irgm1* knockout mice were described previously (Liu *et al*, 2013). About 6–8-week-old male *Irgm1*^{+/+} (wild-type, *n* = 9) and *Irgm1*^{-/-} (*n* = 18, includes GSK583 group) mice were used for the infection. Intraperitoneal infection of *S. flexneri* was performed as reported previously (Yang *et al*, 2014). Briefly, *Shigella* was cultured to the O.D. of 0.4–0.5 and 10⁸ colony-forming units (CFU) were injected intraperitoneally into the mice. GSK583 (30 mg/kg of body weight) is administered intraperitoneally 6 h before the infection. Mice were monitored for body weight, stool consistency, and other clinical parameters. All mice were sacrificed 24-h postinfection. The fecal pathology scores were assigned as follows: stool consistency (0, normal; 1, loose; 2, soft; 3, hard) and color (0, brown; 1, yellow; 2, light green; 3, green).

Pathological scores assigned in colon tissue sections for *Shigella* infection in mice based on the following parameter (Erben *et al*, 2014): hyperplasia (1, less than 25%; 2, mild 26–35%; 3, moderate 36–50%; 4, marked 51% above), loss of goblet cells (1, minimal less than 25%; 2, mild 26–35%; 3, moderate 36–50%; 4, marked 51% above), Leucocytes infiltrate (1, minimal less than 10%; 2, mild 26–35%; 3, moderate 36–50%; 4, marked 51% above).

Dextran sulfate sodium (DSS)-induced colitis model in mice

The 6–7-week-old female C57BL/6 *Irgm1*^{+/+} (*n* = 3) and *Irgm1*^{-/-} (*n* = 6, including GSK583 group) mice were used for the DSS-induced colitis experiment. All the mice were given 2% (wt/vol) DSS dissolved in drinking water for 8 days. The DSS solution was replaced on alternate days. To inhibit the RIPK2, GSK583 (25 mg/kg) was injected intraperitoneally (i.p) 16 h before the start of DSS treatment and also injected intraperitoneally on the 1st, 3rd, 5th, and 7th day. The control group mice were injected

intraperitoneally with vehicle control. Each day, mice were monitored for body weight, stool consistency, and the presence of blood in feces. The stool scores were assigned as follows: 0, well-formed pellets; 1, semisolid; 2, semisolid and not adhere to the anus; 3, liquid and adhere to the anus; and 4, diarrhea. Bleeding scores were assigned as follows; 0, no blood in stool; 1, light faint; 2, clear visible; and 3 gross rectal bleeding. The mice were sacrificed on the 9th day. The entire colon was extracted and measured using the vernier scale. The colon tissue was homogenized in RIPA buffer or Triton X-100 buffer containing PMSF, phosSTOP, and protease inhibitors cocktails and subjected to Western blotting. The tissue was homogenized in trizol for total RNA extraction.

Pathological scores assigned in colon tissue sections for DSS-induced colitis mice based on the following parameter (Erben *et al*, 2014): hyperplasia (1, less than 25%; 2, mild 26–35%; 3, moderate 36–50%; 4, marked 51% above), loss of goblet cells (1, minimal less than 25%; 2, mild 26–35%; 3, moderate 36–50%; 4, marked 51% above), Leucocytes infiltrate (1, minimal less than 10%; 2, mild 26–35%; 3, moderate 36–50%; 4, marked 51% above).

Software and statistical significance

GraphPad Prism 6 was used to analyze and present most of the data. High-content microscopy imaging data were scanned and analyzed using HCS studio and iDEV software, respectively. The number of biological/technical replicates mentioned in each figure legend. The unpaired Student's *t*-test or ordinary one-way ANOVA (Tukey's multiple comparison test) statistical methods are used as appropriate. The *P*-values are mentioned in graphs as appropriate. The densitometry analysis was performed using Image J software.

All the graphical representations are created using Biorender online tool (<https://biorender.com/>).

Data availability

The RNA-seq datasets produced in this study have been deposited in the ArrayExpress database at EMBL-EBI (www.ebi.ac.uk/arrayexpress) under accession numbers E-MTAB-12067 and E-MTAB-12074.

Expanded View for this article is available online.

Acknowledgements

This work is funded by Wellcome Trust/Department of Biotechnology (DBT) India Alliance (IA/15/2/502071) fellowship to SC, extramural grant from the Department of Biotechnology (DBT, BT/PR45223/MED/29/1613/2022) to SC, and DST-Inspire faculty fellowship (DST/INSPIRE/04/2019/001857) to SM. Funding from EMBO Global investigator fellowship to SC is greatly acknowledged. We gratefully acknowledge the support of the Institute of Life Sciences central facilities (Animal house, microscopy, FACS, and sequencing) funded by the Department of Biotechnology (India).

Author contributions

Santosh Chauhan: Conceptualization; data curation; formal analysis; supervision; funding acquisition; investigation; visualization; methodology; writing – original draft; project administration; writing – review and editing.
Subhash Mehto: Data curation; supervision; funding acquisition;

validation; investigation; methodology; writing – review and editing.

Kautilya Kumar Jena: Data curation; formal analysis; investigation; methodology; writing – review and editing. **Rina Yadav:** Data curation; investigation; methodology. **Swatimita Priyadarsini:** Validation; investigation; methodology. **Pallavi Samal:** Investigation; methodology. **Sivaram Krishna:** Investigation; methodology. **Kollori Dhar:** Investigation; methodology. **Ashish Jain:** Investigation; methodology. **Nishant Ranjan Chauhan:** Investigation; methodology. **Krushna Chandra Murmu:** Investigation; methodology. **Ramyasingh Bal:** Investigation; methodology. **Rinku Sahu:** Investigation; methodology. **Pundrik Jaiswal:** Investigation; methodology. **Bhabani Sankar Sahoo:** Investigation; visualization. **Srinivas Patnaik:** Supervision; methodology. **Thomas A Kufer:** Resources; writing – review and editing. **Tor Erik Rusten:** Resources; supervision. **Swati Chauhan:** Data curation; investigation; methodology. **Punit Prasad:** Resources; supervision; visualization.

Disclosure and competing interests statement

The authors declare that they have no conflict of interest.

References

- Cai X, Chen J, Xu H, Liu S, Jiang QX, Halfmann R, Chen ZJ (2014) Prion-like polymerization underlies signal transduction in antiviral immune defense and inflammasome activation. *Cell* 156: 1207–1222
- Caruso R, Warner N, Inohara N, Nunez G (2014) NOD1 and NOD2: signaling, host defense, and inflammatory disease. *Immunity* 41: 898–908
- Caso F, Galozzi P, Costa L, Sfriso P, Cantarini L, Punzi L (2015) Autoinflammatory granulomatous diseases: from Blau syndrome and early-onset sarcoidosis to NOD2-mediated disease and Crohn's disease. *RMD Open* 1: e000097
- Chauhan S, Jena KK, Mehto S, Chauhan NR, Sahu R, Dhar K, Yadav R, Krishna S, Jaiswal P, Chauhan S (2021) Innate immunity and inflammophagy: balancing the defence and immune homeostasis. *FEBS J* 289: 4112–4131
- Chauhan S, Mandell MA, Deretic V (2015) IRGM governs the core autophagy machinery to conduct antimicrobial defense. *Mol Cell* 58: 507–521
- Deretic V (2021) Autophagy in inflammation, infection, and immunometabolism. *Immunity* 54: 437–453
- Dobin A, Davis CA, Schlesinger F, Drenkow J, Zaleski C, Jha S, Batut P, Chaisson M, Gingeras TR (2013) STAR: ultrafast universal RNA-seq aligner. *Bioinformatics* 29: 15–21
- Du Y, Duan T, Feng Y, Liu Q, Lin M, Cui J, Wang RF (2018) LRRC25 inhibits type I IFN signaling by targeting ISG15-associated RIG-I for autophagic degradation. *EMBO J* 37: 351–366
- Ellwanger K, Briesse S, Arnold C, Kienes I, Heim V, Nachbur U, Kufer TA (2019) XIAP controls RIPK2 signaling by preventing its deposition in speck-like structures. *Life Sci Alliance* 2: e201900346
- Erben U, Lodenkemper C, Doerfel K, Spieckermann S, Haller D, Heimesaat MM, Zeitz M, Siegmund B, Kuhl AA (2014) A guide to histomorphological evaluation of intestinal inflammation in mouse models. *Int J Clin Exp Pathol* 7: 4557–4576
- Fabregat A, Jupe S, Matthews L, Sidiropoulos K, Gillespie M, Garapati P, Haw R, Jassal B, Korkminger F, May B et al (2018) The Reactome pathway knowledgebase. *Nucleic Acids Res* 46: D649–D655
- Fridh V, Rittinger K (2012) The tandem CARDs of NOD2: intramolecular interactions and recognition of RIP2. *PLoS ONE* 7: e34375
- Girardin SE, Tournebise R, Mavris M, Page AL, Li X, Stark GR, Bertin J, DiStefano PS, Yaniv M, Sansonetti PJ et al (2001) CARD4/Nod1 mediates NF-kappaB and JNK activation by invasive *shigella flexneri*. *EMBO Rep* 2: 736–742
- Glasser AL, Boudeau J, Barnich N, Perruchot MH, Colombel JF, Darfeuille-Michaud A (2001) Adherent invasive *Escherichia coli* strains from patients with Crohn's disease survive and replicate within macrophages without inducing host cell death. *Infect Immun* 69: 5529–5537
- Goncharov T, Hedayati S, Mulvihill MM, Izrael-Tomasevic A, Zobel K, Jeet S, Fedorova AV, Eidenschek C, deVoss J, Yu K et al (2018) Disruption of XIAP-RIP2 association blocks NOD2-mediated inflammatory signaling. *Mol Cell* 69: 551–565
- Gong Q, Long Z, Zhong FL, Teo DET, Jin Y, Yin Z, Boo ZZ, Zhang Y, Zhang J, Yang R et al (2018) Structural basis of RIP2 activation and signaling. *Nat Commun* 9: 4993
- Haile PA, Votta BJ, Marquis RW, Bury MJ, Mehlmann JF, Singhaus R Jr, Charnley AK, Lakdawala AS, Convery MA, Lipshutz DB et al (2016) The identification and pharmacological characterization of 6-(tert-Butylsulfonyl)-N-(5-fluoro-1H-indazol-3-yl)quinolin-4-amine (GSK583), a highly potent and selective inhibitor of RIP2 kinase. *J Med Chem* 59: 4867–4880
- Han H, Cho JW, Lee S, Yun A, Kim H, Bae D, Yang S, Kim CY, Lee M, Kim E et al (2018) TRRUST v2: an expanded reference database of human and mouse transcriptional regulatory interactions. *Nucleic Acids Res* 46: D380–D386
- Haynes W (2013) Benjamini–Hochberg method. In *Encyclopedia of Systems Biology*, Dubitzky W, Wolkenhauer O, Cho K-H, Yokota H (eds), pp 78–78. New York, NY: Springer New York
- He X, Zhu Y, Zhang Y, Geng Y, Gong J, Geng J, Zhang P, Zhang X, Liu N, Peng Y et al (2019) RNF34 functions in immunity and selective mitophagy by targeting MAVS for autophagic degradation. *EMBO J* 38: e100978
- Henckaerts L, Vermeire S (2007) NOD2/CARD15 disease associations other than Crohn's disease. *Inflamm Bowel Dis* 13: 235–241
- Hou F, Sun L, Zheng H, Skaug B, Jiang QX, Chen ZJ (2011) MAVS forms functional prion-like aggregates to activate and propagate antiviral innate immune response. *Cell* 146: 448–461
- Intemann CD, Thye T, Niemann S, Browne EN, Amanua Chinbuah M, Enimil A, Gyapong J, Osei I, Owusu-Dabo E, Helm S et al (2009) Autophagy gene variant IRGM -261T contributes to protection from tuberculosis caused by *Mycobacterium tuberculosis* but not by *M. africanum* strains. *PLoS Pathog* 5: e1000577
- Jena KK, Mehto S, Nath P, Chauhan NR, Sahu R, Dhar K, Das SK, Kolapalli SP, Murmu KC, Jain A et al (2020) Autoimmunity gene IRGM suppresses cGAS-STING and RIG-I-MAVS signaling to control interferon response. *EMBO Rep* 21: e50051
- Kanazawa N, Okafuji I, Kambe N, Nishikomori R, Nakata-Hizume M, Nagai S, Fuji A, Yuasa T, Manki A, Sakurai Y et al (2005) Early-onset sarcoidosis and CARD15 mutations with constitutive nuclear factor-kappaB activation: common genetic etiology with Blau syndrome. *Blood* 105: 1195–1197
- Kimura T, Watanabe E, Sakamoto T, Takasu O, Ikeda T, Ikeda K, Kotani J, Kitamura N, Sadahiro T, Tateishi Y et al (2014) Autophagy-related IRGM polymorphism is associated with mortality of patients with severe sepsis. *PLoS ONE* 9: e91522
- Kumar S, Jain A, Choi SW, da Silva GPD, Allers L, Mudd MH, Peters RS, Anonsen JH, Rusten TE, Lazarou M et al (2020) Mammalian Atg8 proteins and the autophagy factor IRGM control mTOR and TFEB at a regulatory node critical for responses to pathogens. *Nat Cell Biol* 22: 973–985
- Kumar S, Jain A, Farzam F, Jia J, Gu Y, Choi SW, Mudd MH, Claude-Taupin A, Wester MJ, Lidke KA et al (2018) Mechanism of Stx17 recruitment to autophagosomes via IRGM and mammalian Atg8 proteins. *J Cell Biol* 217: 997–1013
- Laroui H, Yan Y, Narui Y, Ingersoll SA, Ayyadurai S, Charania MA, Zhou F, Wang B, Salaita K, Sitaraman SV et al (2011) L-ala-gamma-D-Glu-meso-

- diaminopimelic acid (DAP) interacts directly with leucine-rich region domain of nucleotide-binding oligomerization domain 1, increasing phosphorylation activity of receptor-interacting serine/threonine-protein kinase 2 and its interaction with nucleotide-binding oligomerization domain 1. *J Biol Chem* 286: 31003–31013
- Lin YC, Chang PF, Lin HF, Liu K, Chang MH, Ni YH (2016) Variants in the autophagy-related gene IRGM confer susceptibility to non-alcoholic fatty liver disease by modulating lipophagy. *J Hepatol* 65: 1209–1216
- Liu B, Gulati AS, Cantillana V, Henry SC, Schmidt EA, Daniell X, Grossniklaus E, Schoenborn AA, Sartor RB, Taylor GA (2013) Irgm1-deficient mice exhibit Paneth cell abnormalities and increased susceptibility to acute intestinal inflammation. *Am J Physiol Gastrointest Liver Physiol* 305: G573–G584
- Liu T, Tang Q, Liu K, Xie W, Liu X, Wang H, Wang RF, Cui J (2016) TRIM11 suppresses AIM2 inflammasome by degrading AIM2 via p62-dependent selective autophagy. *Cell Rep* 16: 1988–2002
- Lopez-Montero N, Enninga J (2018) Diverted recycling-*shigella* subversion of Rabs. *Small GTPases* 9: 365–374
- Love MI, Huber W, Anders S (2014) Moderated estimation of fold change and dispersion for RNA-seq data with DESeq2. *Genome Biol* 15: 550
- Lu A, Li Y, Schmidt FI, Yin Q, Chen S, Fu TM, Tong AB, Ploegh HL, Mao Y, Wu H (2016) Molecular basis of caspase-1 polymerization and its inhibition by a new capping mechanism. *Nat Struct Mol Biol* 23: 416–425
- Lu A, Magupalli VG, Ruan J, Yin Q, Atianand MK, Vos MR, Schroder GF, Fitzgerald KA, Wu H, Egelman EH (2014) Unified polymerization mechanism for the assembly of ASC-dependent inflammasomes. *Cell* 156: 1193–1206
- Lu XC, Tao Y, Wu C, Zhao PL, Li K, Zheng JY, Li LX (2013) Association between variants of the autophagy related gene—IRGM and susceptibility to Crohn's disease and ulcerative colitis: a meta-analysis. *PLoS ONE* 8: e80602
- Massey DC, Parkes M (2007) Genome-wide association scanning highlights two autophagy genes, ATG16L1 and IRGM, as being significantly associated with Crohn's disease. *Autophagy* 3: 649–651
- Mehto S, Chauhan S, Jena KK, Chauhan NR, Nath P, Sahu R, Dhar K, Das SK, Chauhan S (2019a) IRGM restrains NLRP3 inflammasome activation by mediating its SQSTM1/p62-dependent selective autophagy. *Autophagy* 15: 1645–1647
- Mehto S, Jena KK, Nath P, Chauhan S, Kolapalli SP, Das SK, Sahoo PK, Jain A, Taylor GA, Chauhan S (2019b) The Crohn's disease risk factor IRGM limits NLRP3 inflammasome activation by impeding its assembly and by mediating its selective autophagy. *Mol Cell* 73: e427
- Miceli-Richard C, Lesage S, Rybojad M, Prieur AM, Manouvrier-Hanu S, Hafner R, Chamaillard M, Zouali H, Thomas G, Hugot JP (2001) CARD15 mutations in Blau syndrome. *Nat Genet* 29: 19–20
- Nath P, Jena KK, Mehto S, Chauhan NR, Sahu R, Dhar K, Srinivas K, Chauhan S, Chauhan S (2021) IRGM links autoimmunity to autophagy. *Autophagy* 17: 578–580
- Park HH (2019) Caspase recruitment domains for protein interactions in cellular signaling (review). *Int J Mol Med* 43: 1119–1127
- Parkes M, Barrett JC, Prescott NJ, Tremelling M, Anderson CA, Fisher SA, Roberts RG, Nimmo ER, Cummings FR, Soars D et al (2007) Sequence variants in the autophagy gene IRGM and multiple other replicating loci contribute to Crohn's disease susceptibility. *Nat Genet* 39: 830–832
- Pellegrini E, Desfosses A, Wallmann A, Schulze WM, Rehbein K, Mas P, Signor L, Gaudon S, Zenkeviciute G, Hons M et al (2018) RIP2 filament formation is required for NOD2 dependent NF- κ B signalling. *Nat Commun* 9: 4043
- Prabakaran T, Bodda C, Krapp C, Zhang BC, Christensen MH, Sun C, Reinert L, Cai Y, Jensen SB, Skouboe MK et al (2018) Attenuation of cGAS-STING signaling is mediated by a p62/SQSTM1-dependent autophagy pathway activated by TBK1. *EMBO J* 37: e97858
- Ray K, Bobard A, Danckaert A, Paz-Haftel I, Clair C, Ehsani S, Tang C, Sansonetti P, Tran GV, Enninga J (2010) Tracking the dynamic interplay between bacterial and host factors during pathogen-induced vacuole rupture in real time. *Cell Microbiol* 12: 545–556
- Shaid S, Brandts CH, Serve H, Dikic I (2013) Ubiquitination and selective autophagy. *Cell Death Differ* 20: 21–30
- Shi CS, Shenderov K, Huang NN, Kabat J, Abu-Asab M, Fitzgerald KA, Sher A, Kehrl JH (2012) Activation of autophagy by inflammatory signals limits IL-1 β production by targeting ubiquitinated inflammasomes for destruction. *Nat Immunol* 13: 255–263
- Singh SB, Davis AS, Taylor GA, Deretic V (2006) Human IRGM induces autophagy to eliminate intracellular mycobacteria. *Science* 313: 1438–1441
- Singh SB, Ornatowski W, Vergne I, Naylor J, Delgado M, Roberts E, Ponpuak M, Master S, Pilli M, White E et al (2010) Human IRGM regulates autophagy and cell-autonomous immunity functions through mitochondria. *Nat Cell Biol* 12: 1154–1165
- Tanabe T, Chamaillard M, Ogura Y, Zhu L, Qiu S, Masumoto J, Ghosh P, Moran A, Predergast MM, Tromp G et al (2004) Regulatory regions and critical residues of NOD2 involved in muramyl dipeptide recognition. *EMBO J* 23: 1587–1597
- Taniguchi K, Karin M (2018) NF- κ B, inflammation, immunity and cancer: coming of age. *Nat Rev Immunol* 18: 309–324
- Tripathi S, Pohl MO, Zhou Y, Rodriguez-Frandsen A, Wang G, Stein DA, Moulton HM, DeJesus P, Che J, Mulder LC et al (2015) Meta- and orthogonal integration of influenza "OMICS" data defines a role for UBR4 in virus budding. *Cell Host Microbe* 18: 723–735
- Wu B, Hur S (2015) How RIG-I like receptors activate MAVS. *Curr Opin Virol* 12: 91–98
- Wu B, Peisley A, Tetrault D, Li Z, Egelman EH, Magor KE, Walz T, Penczek PA, Hur S (2014) Molecular imprinting as a signal-activation mechanism of the viral RNA sensor RIG-I. *Mol Cell* 55: 511–523
- Wu H, Fuxreiter M (2016) The structure and dynamics of higher-order assemblies: amyloids, signalosomes, and granules. *Cell* 165: 1055–1066
- Xia Q, Wang M, Yang X, Li X, Zhang X, Xu S, Shuai Z, Xu J, Fan D, Ding C et al (2017) Autophagy-related IRGM genes confer susceptibility to ankylosing spondylitis in a Chinese female population: a case-control study. *Genes Immun* 18: 42–47
- Xie T, Peng W, Yan C, Wu J, Gong X, Shi Y (2013) Structural insights into RIP3-mediated necroptotic signaling. *Cell Rep* 5: 70–78
- Xu H, He X, Zheng H, Huang LJ, Hou F, Yu Z, de la Cruz MJ, Borkowski B, Zhang X, Chen ZJ et al (2014) Structural basis for the prion-like MAVS filaments in antiviral innate immunity. *Elife* 3: e01489
- Yang JY, Lee SN, Chang SY, Ko HJ, Ryu S, Kweon MN (2014) A mouse model of shigellosis by intraperitoneal infection. *J Infect Dis* 209: 203–215
- Yao QM, Zhu YF, Wang W, Song ZY, Shao XQ, Li L, Song RH, An XF, Qin Q, Li Q et al (2018) Polymorphisms in autophagy-related gene IRGM are associated with susceptibility to autoimmune thyroid diseases. *Biomed Res Int* 2018: 7959707



License: This is an open access article under the terms of the [Creative Commons Attribution](https://creativecommons.org/licenses/by/4.0/) License, which permits use, distribution and reproduction in any medium, provided the original work is properly cited.